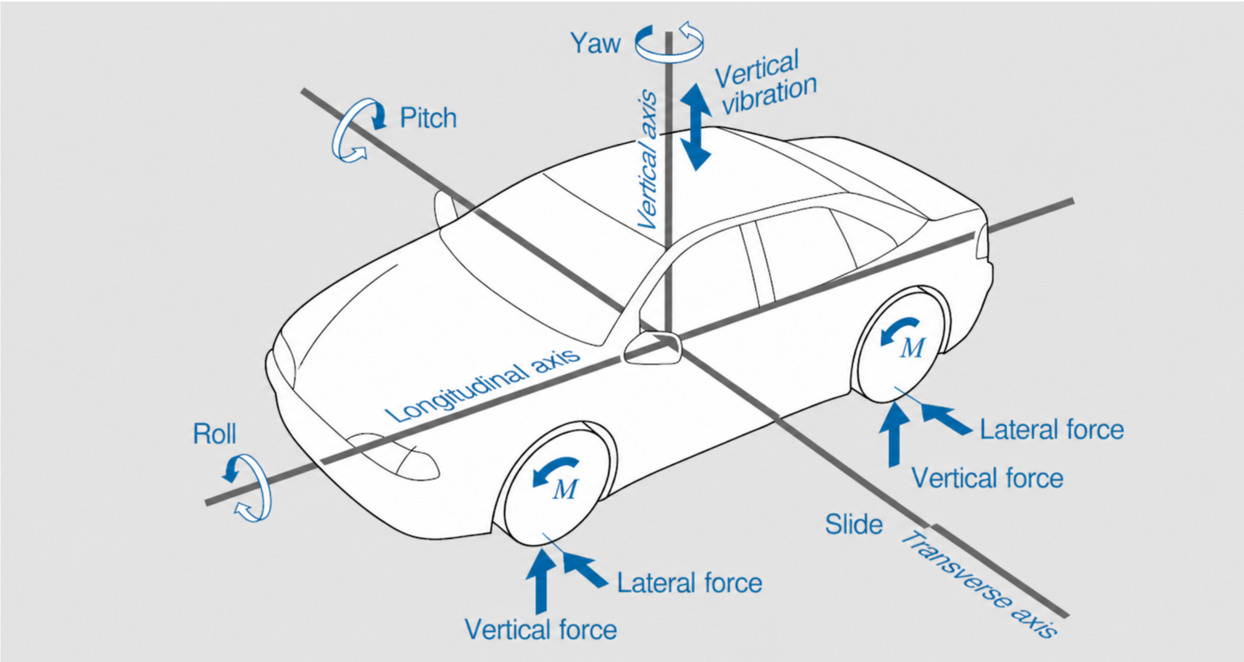

Body Motion Estimation from Non-Dedicated Sensors

A Kalman Filter Based Sensor Fusion Approach for Estimating Vehicle Heave, Roll, and Pitch Accelerations

Master's thesis in MPSYS

Kanishk Nama

DEPARTMENT OF ELECTRICAL ENGINEERING

CHALMERS UNIVERSITY OF TECHNOLOGY
Gothenburg, Sweden 2026
www.chalmers.se

Master's thesis 2026

Body Motion Estimation from Non-Dedicated Sensors

A Kalman Filter Based Sensor Fusion Approach for Estimating Vehicle Heave, Roll, and Pitch Accelerations

Kanishk Nama

Department of Electrocal Engineering
Division of Systems Controls and Mechatronics
Chalmers University of Technology
Gothenburg, Sweden 2026

A Kalman Filter Based Sensor Fusion Approach for Estimating Vehicle Heave, Roll, and Pitch Accelerations
A Deterministic Framework for Generating Vehicle Acceleration Signals Comparable to Dedicated Sensing Systems
KANISHK NAMA

Supervisor: Jayesh Narayan, Volvo Cars
Examiner: Balazs Adam Kulcsar, Department of Electrical Engineering

Master's Thesis 2026
Department of Electrical Engineering
Division of MPSYS
Chalmers University of Technology
SE-412 96 Gothenburg
Telephone +46 31 772 1000

Cover: Kalman Filtering based method to regenerate vehicular accelerations used in the suspension module.

Typeset in LaTeX
Printed by Chalmers Reproservice
Gothenburg, Sweden 2026

Estimating vehicle roll pitch and heave accelerations from classic sensor fusion
A Kalman Filter-based estimation approach
KANISHK NAMA
Department of Electrical Engineering
Chalmers University of Technology

Abstract

Accurate knowledge of vehicle body motion is essential for modern suspension control systems, such as continuously variable damping and air spring control. Traditionally, these systems rely on dedicated accelerometers mounted on the vehicle body. However, modern vehicles already carry inertial sensors within safety-critical subsystems such as the Supplemental Restraint System (SRS), alongside suspension deflection sensors at each wheel. This thesis investigates whether these existing onboard signals can be repurposed to estimate vehicle body accelerations, specifically heave, roll, and pitch, to a standard sufficient for suspension control, without introducing additional hardware.
A Kalman filter-based sensor fusion algorithm is developed, combining SRS IMU measurements with vehicle speed from the CAN bus and suspension deflection signals. The algorithm first estimates vehicle attitude through a linear time-varying Kalman filter that propagates the gravity direction vector using gyroscope measurements and corrects it using compensated lateral and vertical accelerometer readings. The estimated attitude is then used to extract global vertical acceleration from the IMU, which is subsequently fused with suspension-derived body signals in a Kalman-based observer to produce heave, roll, and pitch acceleration estimates. The algorithm was evaluated against ground-truth signals derived from a dedicated accelerometer system currently used at Volvo Cars Corporation. The results demonstrate that heave and pitch accelerations can be reconstructed with strong accuracy across the primary ride frequency band, while roll estimation captures the dominant low-frequency dynamics with more moderate agreement. Overall, the proposed framework shows that SRS-based sensor fusion is a technically viable alternative to dedicated body accelerometers, offering a path toward reduced hardware cost and improved sensor redundancy in production vehicles.

Keywords: Vehicle Dynamics, Rigid Body Dynamics, Sensor Fusion, Kalman Filters, Signal Processing.

Acknowledgements

Over the past six months at Volvo Cars Corporation, I received a great deal of support from my supervisor, Jayesh Narayan. I express my sincere gratitude and appreciation for this support and the opportunity given to me to work on this project. I enjoyed our weekly meetings, during which we discussed different perspectives on the project and the guidance I received, both of which contributed significantly to this thesis work.

I would like to express my deepest gratitude and profound respect to my supervisor and examiner at Chalmers University of Technology, Full Professor Balázs Adam Kulcsár. Throughout this thesis, he has provided not only exceptional technical guidance but also unwavering encouragement, support, and confidence in my abilities. His insightful feedback, patience, and willingness to engage in thoughtful discussions have been invaluable to both the development of this work and my growth as an engineer and researcher. Working under his supervision has been one of the most rewarding experiences of my academic journey, and I consider myself extremely fortunate to have had the opportunity to learn from someone whose mentorship, professionalism, and dedication have left a lasting impression on me. The lessons and values I have gained through his guidance will continue to influence me long after the completion of this thesis.

I would like to express my heartfelt gratitude to my close friends, Hailan Garau Chen, Toshith Manglani, Tushar Choudhary, and Shankho Boron Ghosh. Their constant encouragement, friendship, and emotional support helped me navigate both the challenges and successes of this journey. Whether through words of motivation, thoughtful conversations, or simply being present during difficult times, they provided a support system that made this demanding period significantly more manageable. I would also like to sincerely thank Shekhar Tiwari. Since my arrival in Sweden, he has been much more than a friend; he has been a brotherly figure whose guidance, kindness, and unwavering support helped me adapt to a new environment and overcome many challenges.

Finally, I would like to express my deepest gratitude to my parents and my sister for their unconditional love, sacrifices, and unwavering belief in me throughout my Master's studies. Their constant support, patience, and encouragement gave me the strength to persevere through every challenge and moment of uncertainty. They have always been my foundation, celebrating every success and helping me overcome every setback. This achievement is as much theirs as it is mine, and I am forever grateful for everything they have done for me.

This thesis marks the completion of an important chapter in my life, and I could not have reached this point without all of you standing beside me every step of the way. As a final thought, I would like to quote '*the bee flies anyway*'

Kanishk Nama, Gothenburg, August 2026

List of Acronyms

Below is the list of acronyms that have been used throughout this thesis listed in alphabetical order:

AR	Auto-Regressive
CAN	Controller Area Network
CDC	Continuously Damping Control
CG	Centre of Gravity
DCM	Direction Cosine Matrix
DOF	Degrees of Freedom
ECU	Electronic Control Unit
EKF	Extended Kalman Filter
GPS	Global Positioning System
HPF	High-Pass Filter
IMU	Inertial Measurement Unit
INS	Inertial Navigation System
ISO	International Organization for Standardization
KF	Kalman Filter
LIDAR	Light Detection and Ranging
LPF	Low-Pass Filter
LTV	Linear Time-Varying
MEMS	Micro-Electromechanical Systems
PSD	Power Spectral Density
RMS	Root Mean Square
RMSE	Root Mean Square Error
SRS	Supplemental Restraint System
SUM	Suspension Mechatronics Unit

Nomenclature

Below is the nomenclature of symbols and variables that have been used throughout this thesis.

Scalars and Indices

k	Discrete time step index
t	Continuous time index
Δt	Discrete time step size
g	Gravitational acceleration, $9.81\,\mathrm{m/s^2}$
c_a	Auto-regressive decay constant
σ_G	Gyroscope noise standard deviation
σ_A	Accelerometer noise standard deviation
σ_v	CAN bus speed noise standard deviation
σ_j	Jerk noise parameter
f_c	Filter cut-off frequency
f_{HP}	High-pass filter cut-off frequency
N	Number of samples

Vectors and Matrices

$\mathbf{x}_k$	State vector at time step k
$\mathbf{x}_h$	Heave observer state vector $[z,\ \dot{z},\ \ddot{z}]^\top$
$\mathbf{y}_k$	Measurement vector at time step k
$\mathbf{\Phi}_{k-1}$	State transition matrix
$\mathbf{H}_k$	Observation matrix
$\mathbf{K}_k$	Kalman gain matrix
$\mathbf{P}_k$	Error covariance matrix

$\mathbf{Q}_k$	Process noise covariance matrix
$\mathbf{R}_k$	Measurement noise covariance matrix
$\mathbf{A}$	State transition matrix
$\mathbf{G}$	Process noise input matrix
$\mathbf{R}$	Rotation matrix
$\mathbf{I}$	Identity matrix
$\tilde{\mathbf{y}}_k$	Innovation vector
$\mathbf{S}_k$	Innovation covariance matrix
$\mathbf{\Sigma}_G$	Gyroscope noise covariance matrix
$\mathbf{\Sigma}_A$	Accelerometer noise covariance matrix
$\mathbf{M}_{t,1}$	Measurement noise covariance matrix for Update 1
$\mathbf{x}_k^-$	A priori state estimate
$\mathbf{x}_k^+$	Posterior state estimate after Update 1
$\mathbf{x}_k^{++}$	Posterior state estimate after Update 2
$\mathbf{P}_k^-$	A priori covariance estimate
$\mathbf{P}_k^+$	Posterior covariance estimate after Update 1
$\mathbf{P}_k^{++}$	Posterior covariance estimate after Update 2

Sensor Signals

$\mathbf{y}_{G,t}$	Measured angular velocity from gyroscope, $[G_x, G_y, G_z]^\top$
$\mathbf{y}_{A,t}$	Measured acceleration from accelerometer, $[A_x, A_y, A_z]^\top$
$y_{v,t}$	Vehicle longitudinal speed from CAN bus
$\boldsymbol{\omega}_t$	True angular velocity $[\omega_x, \omega_y, \omega_z]^\top$
$\omega_x, \omega_y, \omega_z$	Angular velocity components about vehicle body axes
$\mathbf{a}_t$	Inertial acceleration due to vehicle motion
a_x, a_y, a_z	Longitudinal, lateral and vertical acceleration components
v_x, v_y, v_z	Vehicle velocity components in the body frame
$\mathbf{g}_t$	Gravitational acceleration in vehicle body frame
$\mathbf{n}_G$	Gyroscope measurement noise
$\mathbf{n}_A$	Accelerometer measurement noise
n_v	CAN bus measurement noise

Vehicle States and Geometry

ϕ	Vehicle roll angle
θ	Vehicle pitch angle
ψ	Vehicle yaw angle
R_{31}	First element of gravity direction state vector
R_{32}	Second element of gravity direction state vector
R_{33}	Third element of gravity direction state vector
$\alpha_{y,t}$	Lateral external acceleration state
$\alpha_{z,t}$	Vertical external acceleration state
z_b	Body heave displacement
$\dot{z}$	Body heave velocity
$\ddot{z}$	Body heave acceleration
$\ddot{z}_{IMU}$	IMU-derived global vertical acceleration
ϕ_{susp}	Suspension-derived roll angle
θ_{susp}	Suspension-derived pitch angle
δ_{FL}	Front-left suspension deflection
δ_{FR}	Front-right suspension deflection
δ_{RL}	Rear-left suspension deflection
δ_{RR}	Rear-right suspension deflection
l_f	Longitudinal distance from CG to front axle
l_r	Longitudinal distance from CG to rear axle
t_f	Front half-track width
t_r	Rear half-track width

Noise Terms and Model Errors

$\mathbf{w}_k$	Process noise vector
$\boldsymbol{\upsilon}_k$	Measurement noise vector
ε_t	External acceleration model error
$\boldsymbol{\Upsilon}_{t,1}$	Measurement noise term for Update 1
$\boldsymbol{\Upsilon}_{t,2}$	Measurement noise term for Update 2
δ_t	Noise associated with the derived Update 2 measurement

Performance Metrics

RMSE	Root mean square error
RMS	Root mean square value

Contents

List of Figures

List of Tables

1
Introduction

Modern vehicles are equipped with a growing number of inertial sensors distributed across various onboard subsystems. Among these, the Supplemental Restraint System (SRS) contains a six-degree-of-freedom IMU that continuously measures vehicle accelerations and angular rates during normal driving, not only during crash events. This raises a practical question: if these sensors are already present and always active, can their data be repurposed to serve other vehicle functions, such as suspension control, without adding new hardware?
This thesis investigates exactly that. The goal is to determine whether SRS IMU data, combined with other existing onboard signals, can replace dedicated body-mounted accelerometers for estimating the vehicle's heave, roll, and pitch accelerations the three dominant body motion quantities required by modern suspension controllers.

1.1 Purpose

To achieve balanced ride comfort, handling, and safety, modern vehicles rely on active and semi-active suspension systems that respond in real time to vehicle body motion. Systems such as continuously variable damping control (CDC) and air spring control depend on accurate, low-latency measurements of suspension deflection and vehicle body accelerations to command their actuators effectively. Traditionally, these inputs are obtained from dedicated accelerometers mounted at carefully chosen locations on the vehicle body.
The current hardware architecture at Volvo Cars Corporation, however, already includes inertial sensors embedded within the SRS subsystem that continuously measure accelerations throughout normal driving. This overlap raises the possibility of consolidating sensing functions, using the SRS IMU in place of the dedicated accelerometer array, thereby reducing hardware cost, wiring complexity, and packaging constraints.
The challenge is that SRS sensors are designed and optimised for crash detection, not motion estimation. They differ from dedicated motion sensors in placement, sampling rate, signal latency, noise characteristics, and signal conditioning. These differences directly affect estimation quality and must be carefully understood and compensated for. The purpose of this work is therefore twofold: to develop a sensor fusion algorithm capable of producing accurate body acceleration estimates from SRS and other existing signals, and to honestly assess where that approach succeeds and where it falls short.

1.2 Architecture Design

The existing approach at Volvo Cars Corporation uses three accelerometers arranged in a predefined geometric configuration on the vehicle body. By combining their measurements through compensation coefficients derived from the sensor positions and vehicle geometry, the system reconstructs the vehicle's heave, roll, and pitch accelerations. This method is computationally efficient and well-suited to the current hardware setup.

[redacted]

Figure 1.1: Existing accelerometer setup at Volvo Cars Corporation.

The proposed architecture replaces this dedicated sensor array with a fusion of signals already available on the vehicle: inertial measurements from the SRS IMU, wheel suspension deflections from the four corner sensors, and longitudinal vehicle speed from the CAN bus. Through state estimation and sensor fusion, these signals are combined to reconstruct the same body accelerations that the dedicated system currently provides.
The key advantage of this approach is that it requires no new hardware. All sensors used are already integrated into the vehicle platform. If successful, the method offers a cost-effective and scalable path toward sensor redundancy, and potentially toward eliminating the dedicated accelerometer array altogether.

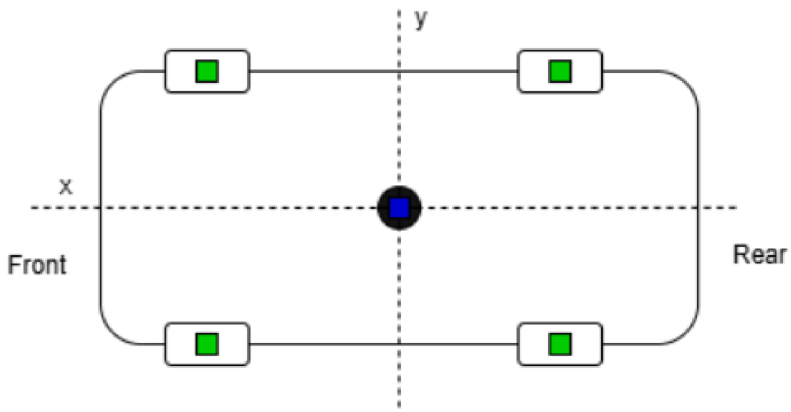

Figure 1.2: Proposed sensor configuration for reconstructing vehicle dominant acceleration signals. The green box represents the suspension deflection sensors; the blue box represents the SRS IMU.

1.3 Scope

The focus of this thesis is specifically on the signal reconstruction problem: can the SRS IMU data, fused with suspension and speed signals, produce body acceleration estimates that are comparable in quality to those from the dedicated accelerometer system? The evaluation is carried out on logged driving data from the Hällered Proving Ground, using the existing dedicated accelerometer outputs as ground truth. The thesis does not address the full integration of this approach into a production suspension controller, nor does it account for communication latency or signal propagation delays between ECUs, these are important practical considerations but are outside the scope of this study.

1.4 Limitations

The observer framework developed in this thesis is based on a linearised model of vehicle dynamics. Nonlinear effects, including road surface irregularities, tyre slip dynamics, wheel hop, and suspension geometry nonlinearities, are not explicitly modelled. The vehicle body is treated as a rigid body, meaning that torsional flexibility of the chassis is neglected. Additionally, since the algorithm is designed to operate at the accelerometer update rate, the effects of inter-ECU signal latency and transmission delays are not accounted for in the current implementation. These simplifications are appropriate for the linear ride frequency range targeted by this study, but they define the operating boundaries within which the results are expected to hold.

2

Literature Review

Estimating vehicle body motion from existing onboard sensors is a well-studied problem, and a substantial body of prior work addresses both the attitude estimation problem and the broader challenge of reconstructing vehicle body accelerations through sensor fusion. This chapter reviews the most relevant contributions, organised around the two core technical problems that this thesis must solve: how to represent and estimate vehicle attitude from a low-cost IMU in a way that is compatible with a linear Kalman filter, and how to compensate for the external accelerations that affect accelerometer measurements during vehicle motion. The chapter closes by surveying approaches to body acceleration reconstruction from suspension sensors, and the performance metrics used to evaluate such estimators.

Attitude Representation

Several parameterisations of vehicle orientation have been used in the literature when constructing Kalman-filter-based attitude estimators. The most intuitive is the Euler angle representation, in which roll, pitch and yaw are used directly as state variables [1]. While conceptually simple, this formulation introduces trigonometric coupling terms into the measurement equations, rendering the filter nonlinear and requiring either linearisation or a computationally heavier nonlinear variant. The quaternion representation avoids singularities entirely and preserves linearity in the filter update equations by encoding orientation as a four-dimensional unit vector [4, 19]. However, it increases the state dimension and requires enforcement of the unit-norm constraint at every time step. The direction cosine matrix (DCM) representation offers a practically attractive middle ground: by retaining only the roll- and pitch-sensitive elements of the DCM as state variables, a linear Kalman filter can be constructed that remains non-singular provided the vehicle never reaches 90° of inclination [2, 3]. For a road vehicle operating under normal driving conditions, this constraint is never approached, making the DCM approach the most suitable choice for the present work.

Gyroscope Drift and the Need for Attitude Correction

Regardless of the orientation parameterisation chosen, a gyroscope alone cannot maintain a reliable attitude estimate over time. MEMS-grade gyroscopes, which are the only cost-viable option for mass-produced vehicles, exhibit a time-varying bias whose integral drifts unboundedly without external correction [7]. High-precision fibre-optic and ring-laser gyroscopes achieve angle random walk values below $0.001\ \mathrm{deg}/\sqrt{\mathrm{hr}}$ [6], but their cost renders them entirely impractical for automotive use. External references such as cameras, LiDAR, and GPS have been shown to correct gyroscope drift effectively [5], but again at a cost in hardware and computation that is unjustifiable when equivalent onboard sensors are already present.

Accelerometers represent the natural low-cost complement to the gyroscope. When the vehicle is stationary or in steady-state motion, the accelerometer output is dominated by gravity and provides a direct attitude reference. However, any vehicle acceleration contaminates this gravity measurement with kinematic contributions, corrupting the attitude update unless these external accelerations are first removed. This external acceleration compensation problem is central to the design of any IMU-based attitude estimator for moving vehicles, and it has received considerable attention in the literature.

External Acceleration Compensation Strategies

The simplest approach to handling external accelerations is the threshold method, in which the filter switches between two operating modes based on whether the accelerometer norm is close to $9.81\ \mathrm{m/s^2}$ [8]. When the vehicle is judged to be in a quasi-static state, the accelerometer provides the full attitude correction; when it is deemed dynamic, the filter relies solely on the gyroscope. The fundamental weakness of this approach is that all gyroscope-only intervals accumulate drift, and the binary static-or-dynamic classification is inherently sensitive to sensor noise and misclassification. Any extended dynamic manoeuvre therefore leads to a progressive loss of attitude accuracy that cannot be recovered until the vehicle returns to a nearly static condition.

A more nuanced strategy uses the magnitude of the Kalman filter innovation to estimate the degree of external acceleration contamination and reduces the weight assigned to the accelerometer correction accordingly [9]. This avoids the hard switching of the threshold approach and eliminates misclassification errors, but the fundamental limitation remains: whenever external acceleration is judged to be large, the attitude estimate falls back onto the gyroscope and begins to drift. The approach is therefore unsuitable for driving scenarios that involve sustained lateral or longitudinal accelerations.

Modelling external acceleration as a first-order autoregressive process and estimating it adaptively within the filter framework offers a step forward in accuracy [10]. By treating the unknown external acceleration as an additional filter state, the approach can track slowly varying acceleration disturbances without switching to a gyroscope-only mode. However, the simplified first-order dynamics assumed for the external acceleration state break down under the rapid and prolonged acceleration disturbances typical of road vehicle manoeuvres, and the method has been shown to perform poorly in precisely these conditions [10].

A more physically grounded strategy, proposed in [3] and further developed in [20], computes the dominant external acceleration components directly from kinematic relationships using vehicle speed and gyroscope measurements. Centripetal accelerations during cornering and pitching can be expressed as products of the forward speed and the measured angular rate, both of which are available from the CAN bus and the IMU respectively. The residual lateral and vertical accelerations that cannot be directly computed are modelled as slowly varying states updated by a low-pass filter, avoiding the circular dependency that arises when the acceleration estimate is derived from the same signal it is intended to correct. This approach provides robust attitude correction even during dynamic driving conditions without requiring any nonlinear vehicle model inputs, and it forms the conceptual foundation for the external acceleration compensation strategy adopted in this thesis. The framework proposed in [3] is the primary reference for the attitude estimator developed in Chapter 4.

An alternative class of methods estimates external acceleration through a more complete vehicle dynamics model. Chen et al. [11] and Oh and Choi [12] estimated longitudinal and lateral velocity using wheel speed sensors and a bicycle model, from which the kinematic accelerations can be derived and removed from the IMU signal. While the reported accuracy is good, these methods require tyre slip angle estimates and other inputs from nonlinear vehicle subsystems, introducing model dependencies and computational overhead that make them poorly suited to the linear, real-time estimation framework targeted here.

Body Acceleration Estimation from Suspension and IMU

Beyond attitude estimation, several studies have addressed the reconstruction of vehicle body accelerations directly. [13] demonstrated that fusing a six-degree-of-freedom IMU with standard production car sensors, including wheel speed, steering angle, and suspension level sensors, within a linear Kalman filter framework achieves sufficient accuracy for attitude and velocity estimation under both normal urban driving and harsh dynamic manoeuvres. That work is closely related in spirit to the present thesis, though it focuses on velocity and attitude rather than body accelerations for suspension control.

The method of computing roll and pitch rates directly from suspension corner deflections was proposed by [16], using vehicle geometry and rigid body kinematics to relate corner height differences to angular motion. This provides an independent low-frequency angular reference that is complementary to the high-frequency sensitivity of the IMU, and it is a key building block of the roll and pitch observers developed in Chapter 4. Kinematic constant-acceleration models, in which the body acceleration is propagated as a near-constant state driven by a jerk process noise input, have been widely used to estimate accelerations from onboard sensor combinations [14, 15]. These models provide a computationally efficient state transition structure and form the basis of the observer designs presented in this work.

At the more complex end of the spectrum, [17] applied a full seven-degree-of-freedom vehicle model within an Unscented Kalman Filter to capture suspension nonlinearities and estimate body accelerations. While this yields accurate results in simulation, the method involves significant computational cost and introduces estimation delays that are undesirable in a real-time suspension control context. The present thesis deliberately avoids this level of model complexity, accepting the limitations of a linear framework in exchange for computational efficiency and implementability on production ECUs.

Performance Metrics and Evaluation Standards

Evaluating the quality of body acceleration estimates requires metrics that capture both the amplitude accuracy and the dynamic fidelity of the estimated signal. The root mean square error (RMSE) is the most widely used scalar metric in vehicle dynamics estimation literature [13, 17], providing a straightforward measure of absolute estimation error. The normalised RMSE (NRMSE), obtained by dividing the RMSE by the root mean square value of the reference signal, allows meaningful comparison across axes and datasets with differing signal amplitudes. The Pearson correlation coefficient complements the RMSE by quantifying waveform similarity independently of amplitude scaling, and is commonly reported alongside RMSE in sensor fusion evaluation studies [21].

Frequency-domain analysis provides additional insight that time-domain metrics alone cannot capture. Power spectral density (PSD) comparison reveals whether the observer reproduces the spectral content of the reference signal across the relevant frequency range, and the mean squared coherence function quantifies the linear relationship between estimated and reference signals as a function of frequency. These metrics are particularly important in the context of ride comfort, where the human body responds selectively to vibration in specific frequency bands.

The standard framework for ride-comfort-oriented evaluation is provided by ISO 2631-1:1997 [24], which defines frequency-weighting filters that model the sensitivity of the human body to whole-body vibration. The W_k filter applies to vertical (heave) acceleration, while the W_e and W_d filters apply to pitch and roll accelerations respectively. By computing the RMS of the ISO-weighted estimation error, performance can be expressed in terms that are directly relevant to the perceived ride quality experienced by vehicle occupants. This perceptually motivated metric captures whether the observer accurately reproduces the vibration content that matters most for suspension control, even when broadband error metrics suggest moderate overall accuracy. The vehicle body axis conventions and coordinate definitions used throughout this thesis follow ISO 8855:2011 [23].

3

Theory

Each sensor used in this thesis, the SRS IMU, the suspension deflection sensors, and the CAN bus speed signal, provides only a partial and noisy view of the vehicle body motion. No single source is sufficient on its own: the IMU drifts without correction, the suspension sensors are dominated by road noise at high frequencies, and the vehicle speed signal will not carry attitude information always. To reconstruct heave, roll, and pitch accelerations from this combination of imperfect measurements, appropriate filtering and estimation tools must be employed.

This chapter introduces the four signal processing and estimation techniques that underpin the methodology developed in Chapter 4. The Kalman filter forms the core estimation engine and is used in three distinct roles: the attitude estimator, the heave observer, and the roll and pitch observer. The low-pass filter is used to pre-filter IMU channels and the CAN bus speed signal prior to estimation. The Savitzky-Golay filter is used to differentiate filtered angular rate signals into angular accelerations without excessive noise amplification. The high-pass filter is used to remove the residual low-frequency gravity bias from the IMU-derived vertical acceleration signal.

3.1 The Kalman Filter

The Kalman filter is a recursive estimator that produces optimal state estimates for linear systems subject to Gaussian process and measurement noise [22]. It operates in two alternating stages. In the prediction stage, the filter propagates the current state estimate forward in time using a physics-based process model. In the correction stage, newly arrived sensor measurements are used to update the predicted state, pulling the estimate toward the observed data in proportion to the relative confidence assigned to the model and the sensor. The result is a statistically optimal combination of prediction and observation that minimises the posterior estimation error covariance [21].

The filter continuously balances two sources of information: the mathematical model, which captures the known dynamics of the system, and the sensor measurements, which carry direct but noisy observations of the state. When the model is trusted more than the sensor, the filter weights the prediction heavily; when the sensor is trusted more, the measurement dominates. This balance is governed by the Kalman gain, which is computed automatically from the process and measurement noise covariances at each time step. As a result, the estimated states lie between the model prediction and the measured observations, producing smooth and consistent estimates even in the presence of significant sensor noise and disturbances [22].

System Model

Consider a discrete-time linear stochastic system of the form

$$\mathbf{x}_k = \mathbf{\Phi}_{k-1}\,\mathbf{x}_{k-1} + \mathbf{w}_{k-1}, \tag{3.1}$$
$$\mathbf{y}_k = \mathbf{H}_k\,\mathbf{x}_k + \boldsymbol{v}_k, \tag{3.2}$$

where $\mathbf{x}_k \in \mathbb{R}^n$ is the state vector at time step k, $\mathbf{y}_k \in \mathbb{R}^m$ is the measurement vector, $\mathbf{\Phi}_{k-1} \in \mathbb{R}^{n\times n}$ is the state transition matrix, and $\mathbf{H}_k \in \mathbb{R}^{m\times n}$ is the observation matrix. The terms $\mathbf{w}_{k-1}$ and $\boldsymbol{v}_k$ are the process noise and measurement noise respectively, which are assumed to be zero-mean, mutually uncorrelated white Gaussian process noise where $\mathbf{Q}_k \in \mathbb{R}^{n\times n}$ is the process noise covariance matrix and $\mathbf{R}_k \in \mathbb{R}^{m\times m}$ is the measurement noise covariance matrix.

$$\mathbf{w}_k \sim \mathcal{N}(\mathbf{0},\, \mathbf{Q}_k), \tag{3.3}$$
$$\boldsymbol{v}_k \sim \mathcal{N}(\mathbf{0},\, \mathbf{R}_k), \tag{3.4}$$

Time Update (Prediction)

Given the posterior state estimate $\mathbf{x}_{k-1}^{+}$ and its error covariance $\mathbf{P}_{k-1}^{+}$ from the previous time step, the filter propagates both quantities forward using the process model:

$$\mathbf{x}_k^{-} = \mathbf{\Phi}_{k-1}\,\mathbf{x}_{k-1}^{+}, \tag{3.5}$$
$$\mathbf{P}_k^{-} = \mathbf{\Phi}_{k-1}\,\mathbf{P}_{k-1}^{+}\,\mathbf{\Phi}_{k-1}^{\top} + \mathbf{Q}_{k-1}. \tag{3.6}$$

The superscript $(-)$ denotes the *a priori* (predicted) quantity, before any measurement at step k has been incorporated.

Measurement Update (Correction)

When a new measurement $\mathbf{y}_k$ becomes available, the *a priori* estimate is corrected. The innovation, defined as the difference between the actual measurement and the predicted measurement, is

$$\tilde{\mathbf{y}}_k = \mathbf{y}_k - \mathbf{H}_k\,\mathbf{x}_k^{-}, \tag{3.7}$$

and the innovation covariance is

$$\mathbf{S}_k = \mathbf{H}_k\,\mathbf{P}_k^{-}\,\mathbf{H}_k^{\top} + \mathbf{R}_k. \tag{3.8}$$

The Kalman gain $\mathbf{K}_k$ determines how much weight is assigned to the new measurement relative to the prediction:

$$\mathbf{K}_k = \mathbf{P}_k^- \, \mathbf{H}_k^\top \, \mathbf{S}_k^{-1}. \tag{3.9}$$

The posterior state estimate and error covariance are then updated as

$$\mathbf{x}_k^+ = \mathbf{x}_k^- + \mathbf{K}_k \, \tilde{\mathbf{y}}_k, \tag{3.10}$$
$$\mathbf{P}_k^+ = (\mathbf{I} - \mathbf{K}_k \, \mathbf{H}_k) \, \mathbf{P}_k^-. \tag{3.11}$$

The gain $\mathbf{K}_k$ is derived by minimising $\mathbf{P}_k^+$, that is, the total posterior state uncertainty. When $\mathbf{R}_k$ is small (high sensor confidence), $\mathbf{K}_k$ is large and the filter trusts the measurement. When $\mathbf{Q}_k$ is small (high model confidence), $\mathbf{P}_k^-$ remains small and the filter relies more heavily on the prediction.

Sequential Measurement Updates

When two independent measurement sources are available at the same time step, both can be incorporated sequentially rather than in a single joint update [14]. Given measurements $\mathbf{y}_{k,1}$ and $\mathbf{y}_{k,2}$ with associated matrices $(\mathbf{H}_1, \mathbf{R}_1)$ and $(\mathbf{H}_2, \mathbf{R}_2)$, the standard update equations are applied twice in succession:

1. Apply Update 1 using $(\mathbf{y}_{k,1}, \, \mathbf{H}_1, \, \mathbf{R}_1)$ to obtain $\mathbf{x}_k^+$ and $\mathbf{P}_k^+$.
2. Apply Update 2 using $(\mathbf{y}_{k,2}, \, \mathbf{H}_2, \, \mathbf{R}_2)$ to $\mathbf{x}_k^+$ and $\mathbf{P}_k^+$, yielding $\mathbf{x}_k^{++}$ and $\mathbf{P}_k^{++}$.

This is equivalent to a joint update when the two measurement noise vectors are uncorrelated, while avoiding the need to invert a larger combined innovation covariance matrix. This sequential structure is used in the attitude estimator developed in Section 4.2, where the lateral and vertical accelerometer updates are applied one after the other at each time step.

3.2 Low-Pass Filter

A low-pass filter attenuates high-frequency content in a signal while preserving its low-frequency components. It smooths the signal and suppresses broadband noise without distorting the underlying slow-varying dynamics of interest. The transfer function of a first-order low-pass filter is

$$H(s) = \frac{1}{1 + \dfrac{s}{\omega_c}}, \tag{3.12}$$

where $H(s)$ is the filter transfer function and ω_c is the cutoff angular frequency. The cutoff frequency in Hz is

$$f_c = \frac{\omega_c}{2\pi}. \tag{3.13}$$

Frequencies below f_c are preserved, while frequencies above f_c are progressively attenuated. In this thesis, low-pass filters are applied to the IMU accelerometer and gyroscope channels at 25 Hz, and to the CAN bus vehicle speed signal at 3 Hz, to suppress digitisation noise prior to estimation.

3.3 Savitzky-Golay Filter

The Savitzky-Golay filter smooths a signal and reduces noise while preserving the shape of important signal features such as peaks and derivatives. It operates by fitting a low-order polynomial to a sliding window of data points using the method of least squares, and evaluating the polynomial at the central point of the window. The filtered output is

$$y_i = \sum_{j=-m}^{m} c_j \, x_{i+j}, \tag{3.14}$$

where x_{i+j} are the input data points within the window of half-width m, c_j are the coefficients determined by the polynomial fitting procedure, and y_i is the filtered output at sample i. Unlike a simple moving-average filter, the Savitzky-Golay filter preserves the shape of the signal more faithfully because it fits a polynomial rather than computing a flat average. In this thesis, a Savitzky-Golay derivative filter is used to numerically differentiate the low-pass-filtered IMU angular rate signals to obtain angular acceleration estimates, providing noise-robust differentiation while preserving the derivative signal shape.

3.4 High-Pass Filter

A high-pass filter attenuates low-frequency components and allows high-frequency components to pass through. It is used to remove slow-varying offsets and baseline drift from a signal. The transfer function of a first-order high-pass filter is

$$H(s) = \frac{\dfrac{s}{\omega_c}}{1 + \dfrac{s}{\omega_c}}, \tag{3.15}$$

where ω_c is the cutoff angular frequency. The cutoff frequency in Hz is

$$f_c = \frac{\omega_c}{2\pi}. \tag{3.16}$$

Frequencies above f_c are preserved, while frequencies below f_c are attenuated. In this thesis, a high-pass filter with a cutoff of 0.05 Hz is applied to the IMU-derived global vertical acceleration signal to remove the residual low-frequency bias that arises from imperfect gravity compensation in the attitude estimator.

4
Methodology

This chapter presents the complete estimation framework developed to reconstruct vehicle body heave, roll, and pitch accelerations from existing onboard sensors. The framework consists of two interconnected stages. The first stage is an attitude estimator that determines the vehicle's roll and pitch angles using measurements from the SRS IMU and the CAN bus speed signal. The second stage comprises three Kalman-based observers, one for heave, one for roll, and one for pitch, that fuse the estimated attitude with suspension deflection signals to produce the final body acceleration estimates.
The following sections describe the sensor models, coordinate conventions, filtering techniques, and estimation algorithms employed at each stage.

4.1 Sensors and Measurements

The proposed sensor fusion framework draws on four measurement sources already present in the vehicle. Each sensor provides partial information about the vehicle body motion; it is only through their fusion that accurate estimates of heave, roll, and pitch acceleration become possible. The sensors and their measurement models are described below.

- **Dedicated Accelerometers**
  As discussed previously in Chapter 1, the current approach for calculating vehicle body accelerations relies on a set of accelerometers geometrically distributed across the vehicle chassis. By combining the measurements from these sensors using predefined geometric relationships and compensation coefficients, the vehicle's heave, roll, and pitch accelerations can be determined. In this study, the accelerations obtained from the existing accelerometer-based system are treated as the reference measurements, or ground truth, against which the performance of the proposed sensor fusion estimation framework is evaluated.
- **IMU-Accelerometer**
  The accelerometer integrated within the SRS ECU IMU measures the specific forces acting on the vehicle body along three orthogonal axes. These measurements capture both the dynamic accelerations generated by vehicle motion and the gravitational acceleration component, making them a valuable source of information for vehicle state estimation. In the proposed sensor fusion framework, the accelerometer signals are utilized to estimate the vehicle's roll and pitch attitudes by exploiting the relationship between gravity and

sensor orientation. Furthermore, the measured accelerations contribute to the reconstruction of vehicle body motions and provide essential information for the estimation of vertical, roll, and pitch accelerations used in the suspension control and ride dynamics analysis.

$$y_{A,t} = g_t + a_t + n_A \tag{4.1}$$

- **IMU-Gyrometer**
  The SRS ECU is equipped with a six-degree-of-freedom (6-DOF) inertial measurement unit (IMU), comprising a three-axis accelerometer and a three-axis gyroscope. This sensor provides measurements of the vehicle's linear accelerations and angular rates, thereby capturing both the translational and rotational dynamics of the vehicle body. These measurements form a key input to the proposed sensor fusion framework and are utilized for vehicle attitude estimation and motion reconstruction.

$$y_{G,t} = \boldsymbol{\omega}_t + n_G \tag{4.2}$$

- **Suspension Deflection Sensors**
  The suspension deflection sensors are mounted at each wheel suspension assembly and are used to measure the relative displacement between the sprung and unsprung masses. These sensors operate as angular position sensors attached to the suspension mechanism, where changes in suspension geometry are first measured as angular displacements. The conversion from angular displacement to linear suspension travel is performed internally using predefined kinematic relationships, allowing the sensors to directly output compensated vertical deflection measurements at their respective mounting locations. These measurements provide valuable information regarding the vertical dynamics of the vehicle and are utilized within the proposed sensor fusion framework for motion estimation.

$$\delta = z_b + \theta x + \phi y \tag{4.3}$$

- **Vehicle Speed**
  The vehicle speed is obtained from signals available on the CAN bus and represents the longitudinal velocity of the vehicle. This signal is computed by the vehicle's onboard systems using information from multiple sources, such as wheel speed sensors and other vehicle dynamics measurements, to provide a robust estimate of the vehicle's forward speed. Within the proposed sensor fusion framework, the vehicle speed serves as an important input for modeling vehicle dynamics and improving the accuracy of the state estimation process.

$$y_{v,t} = v_t + n_v \tag{4.4}$$

The symbols appearing in the measurement models above are defined in Table 4.1.

Table 4.1: Symbol definitions for the sensor measurement models.

Symbol	**Meaning**
$\mathbf{y}_{G,t} = [G_x, G_y, G_z]^\top$	Measured angular velocity from gyroscope
$\boldsymbol{\omega}_t = [\omega_x, \omega_y, \omega_z]^\top$	True angular velocity (unknown)
$\mathbf{n}_G$	Gyroscope noise, zero-mean Gaussian, variance σ_G^2 per axis
$\mathbf{y}_{A,t} = [A_x, A_y, A_z]^\top$	Measured specific force from accelerometer
$\mathbf{g}_t = g\,\mathbf{x}_t$	Gravitational acceleration vector in the vehicle body frame
$\mathbf{a}_t = [a_x, a_y, a_z]^\top$	Inertial acceleration due to vehicle motion
$\mathbf{n}_A$	Accelerometer noise, zero-mean Gaussian, variance σ_A^2 per axis
$y_{v,t}$	Vehicle longitudinal speed from CAN bus
v_t	True vehicle speed
n_v	CAN bus measurement noise
δ	Compensated vertical suspension deflection at a single corner

4.2 Attitude Estimator: Roll and Pitch from the IMU

Before vertical body acceleration can be extracted from the IMU, the orientation of the vehicle must be known. The IMU accelerometer measures specific force, which is the sum of gravitational and inertial contributions and depends on the current body attitude. Even a small error in the estimated roll or pitch angle produces a measurable gravity projection onto the vertical axis, introducing a bias into the heave estimate. Accurate attitude estimation is therefore a prerequisite for heave recovery and constitutes a significant part of the sensor fusion framework.

Coordinate Convention

The vehicle body axes follow the ISO 8855 convention [23]: x points forward, y points left, and z points upward. The roll angle ϕ is the rotation about the x-axis, and the pitch angle θ is the rotation about the y-axis. Heave refers to translational motion along the z-axis. The convention is illustrated in Figure 4.1.

Sensor Suite and Measurement Models

The attitude estimator fuses measurements from three of the four sources described in Section 4.1: the [redacted] (tri-axial accelerometer and tri-axial gyroscope), the longitudinal vehicle speed from the CAN bus, and the four suspension deflection sensors. The measurement equations at time step t in the vehicle body frame are

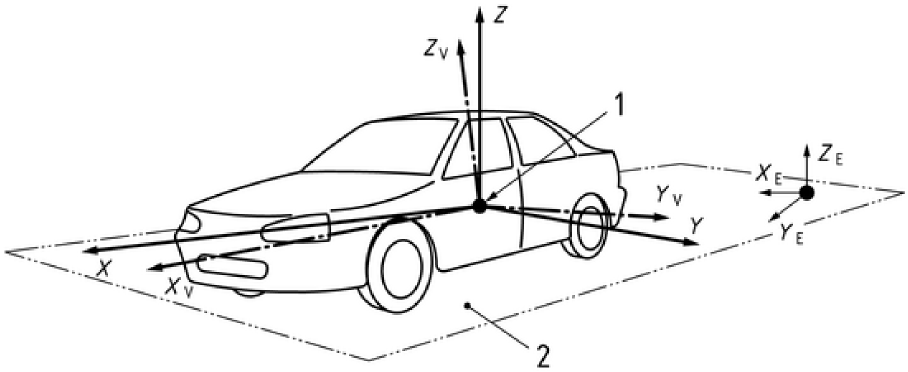

Figure 4.1: ISO 8855 sign convention for vehicle body axes [23].

$$
\begin{aligned}
\mathbf{y}_{G,t} &= \boldsymbol{\omega}_t + \mathbf{n}_G && \text{(gyroscope: angular rate)}, && (4.5)\\
\mathbf{y}_{A,t} &= \mathbf{g}_t + \mathbf{a}_t + \mathbf{n}_A && \text{(accelerometer: specific force)}, && (4.6)\\
y_{v,t} &= v_t + n_v && \text{(CAN bus: forward speed)}, && (4.7)\\
\delta &= z_b + \theta\, x + \phi\, y && \text{(suspension: corner height)}, && (4.8)
\end{aligned}
$$

where $\mathbf{g}_t$ is the gravity vector in the body frame, $\mathbf{a}_t$ is the vehicle kinematic acceleration, and $\mathbf{n}_G$, $\mathbf{n}_A$, n_v are zero-mean Gaussian noise terms with standard deviations taken from the IMU datasheet,

$$\sigma_G = 3.49 \times 10^{-4}\ \text{rad/s}, \qquad \sigma_A = 0.02\ \text{m/s}^2, \qquad \sigma_v = 0.10\ \text{m/s}. \tag{4.9}$$

All IMU channels are low-pass filtered at $f_{\text{LP,IMU}} = 25\,\text{Hz}$ and the CAN bus speed is low-pass filtered at $f_{\text{LP,spd}} = 3\,\text{Hz}$ prior to estimation to suppress broadband digitisation noise (see Section 3.2).

Gravity Direction State and Filter Design

The three-dimensional direction cosine matrix (DCM) $\mathbf{R}$ relates the body frame to the navigation frame. Since a ground vehicle operating under normal conditions never approaches 90° of roll or pitch, the Euler angle representation remains non-singular and the full 3×3 DCM can be parameterised by the roll ϕ, pitch θ, and yaw ψ:

$$\mathbf{R} = \begin{bmatrix} c_\psi c_\theta & c_\psi s_\theta s_\phi - s_\psi c_\phi & c_\psi s_\theta c_\phi + s_\psi s_\phi \\ s_\psi c_\theta & s_\psi s_\theta s_\phi + c_\psi c_\phi & s_\psi s_\theta c_\phi - c_\psi s_\phi \\ -s_\theta & c_\theta s_\phi & c_\theta c_\phi \end{bmatrix}, \tag{4.10}$$

where c and s abbreviate (cosine) cos and (sine) sin. The third row of $\mathbf{R}$ depends only on ϕ and θ, not on ψ. This property is key: it allows attitude estimation without a magnetometer or any other yaw reference, since the roll and pitch information is entirely contained in the third row.

The unit gravity direction vector in the body frame is chosen as the filter state:

$$\mathbf{x}_t = -\frac{\mathbf{g}_b}{g} = \begin{bmatrix} \sin\theta \\ -\cos\theta\sin\phi \\ -\cos\theta\cos\phi \end{bmatrix}, \tag{4.11}$$

where $g = 9.81\,\mathrm{m/s^2}$ and g_b is the gravity direction in the three directions. The sign convention follows from the initialisation $\mathbf{x}_0 = -\mathbf{a}_0/\|\mathbf{a}_0\|$, where $\mathbf{a}_0$ is the mean stationary accelerometer reading making it a unit vector that points in the measured gravity direction. At a level vehicle attitude, this gives $\mathbf{x} \approx [0,\,0,\,-1]^T$, consistent with the ISO 8855 upward z-axis convention in which a stationary accelerometer reads $+g$. The roll and pitch angles are recovered from the estimated state as

$$\phi = \operatorname{atan2}(-x_2,\,-x_3), \qquad \theta = \operatorname{atan2}\Big(x_1,\,\sqrt{x_2^2+x_3^2}\Big). \tag{4.12}$$

Prediction Step: Gyroscope-Driven State Propagation

The gravity direction vector evolves as the vehicle rotates. The DCM is advanced by one time step using the measured angular velocity via the first-order discrete approximation

$$\mathbf{R}_t = \mathbf{R}_{t-1}\Big(\mathbf{I}_3 + \Delta t\,[\boldsymbol{\omega}]_\times\Big), \tag{4.13}$$

where $[\boldsymbol{\omega}]_\times$ is the skew-symmetric cross-product matrix of $\boldsymbol{\omega} = [\omega_x,\,\omega_y,\,\omega_z]^T$:

$$[\boldsymbol{\omega}]_\times = \begin{bmatrix} 0 & -\omega_z & \omega_y \\ \omega_z & 0 & -\omega_x \\ -\omega_y & \omega_x & 0 \end{bmatrix}. \tag{4.14}$$

This approximation is valid for small Δt. Extracting only the third row of the updated DCM, the state propagation becomes

$$\mathbf{x}_t = \boldsymbol{\Phi}_{t-1}\,\mathbf{x}_{t-1} + \mathbf{w}_{t-1}, \tag{4.15}$$

where the state transition matrix, recomputed at each step from the gyroscope reading $\mathbf{y}_{G,t-1}$, is

$$\boldsymbol{\Phi}_{t-1} = \mathbf{I}_3 - \Delta t\,[\mathbf{y}_{G,t-1}]_\times, \tag{4.16}$$

and the process noise is

$$\mathbf{w}_{t-1} = \Delta t\,[\mathbf{x}_{t-1}]_\times\,\mathbf{n}_G. \tag{4.17}$$

Note the minus sign in Equation (4.16): the state corresponds to the transpose of the third row of $\mathbf{R}$, which introduces a sign reversal relative to Equation (4.13). Because $\boldsymbol{\Phi}_{t-1}$ is recomputed at every iteration from the current gyroscope reading, the filter is a linear time-varying (LTV) Kalman filter. The recursive predict–update structure from Chapter 3 is unchanged; only $\boldsymbol{\Phi}_{t-1}$ and $\mathbf{Q}_{t-1}$ are updated at each step.

The process noise covariance follows from Equation (4.17):

$$\mathbf{Q}_{t-1} = \mathbb{E}[\mathbf{w}_{t-1}\mathbf{w}_{t-1}^T] = \Delta t^2 \, [\mathbf{x}_{t-1}]_\times \, \boldsymbol{\Sigma}_G \, [\mathbf{x}_{t-1}]_\times^T, \qquad \boldsymbol{\Sigma}_G = \sigma_G^2 \, \mathbf{I}_3, \tag{4.18}$$

where the skew-symmetric identity $[\mathbf{x}]_\times^T = -[\mathbf{x}]_\times$ has been applied. Although $\mathbf{w}_{t-1}$ is state-dependent, this does not violate the Kalman filter assumptions, as the state is treated as a deterministic quantity at each conditioning step [18]. The prediction step proceeds as

$$\mathbf{x}_t^- = \boldsymbol{\Phi}_{t-1} \, \mathbf{x}_{t-1}, \qquad \mathbf{P}_t^- = \boldsymbol{\Phi}_{t-1} \, \mathbf{P}_{t-1} \, \boldsymbol{\Phi}_{t-1}^T + \mathbf{Q}_{t-1}. \tag{4.19}$$

External Acceleration Compensation

The accelerometer output $\mathbf{y}_{A,t} = \mathbf{g}_t + \mathbf{a}_t + \mathbf{n}_A$ contains the vehicle kinematic acceleration $\mathbf{a}_t$ in addition to gravity. To isolate $\mathbf{g}_t$ for the attitude update, $\mathbf{a}_t$ must be removed. In a rotating body frame, the three components of $\mathbf{a}_t$ are related to the vehicle velocity and angular rates by

$$a_{x,t} = \dot{v}_{x,t} - \omega_{z,t} v_{y,t} + \omega_{x,t} v_{z,t}, \tag{4.20}$$

$$a_{y,t} = \dot{v}_{y,t} + \omega_{z,t} v_{x,t} - \omega_{y,t} v_{z,t}, \tag{4.21}$$

$$a_{z,t} = \dot{v}_{z,t} - \omega_{x,t} v_{x,t} + \omega_{y,t} v_{y,t}. \tag{4.22}$$

The practical removability of each axis is summarised in Table 4.2.

Table 4.2: External acceleration compensation strategy by axis.

Axis	Dominant term	Treatment
Longitudinal (x)	$\dot{v}_{x,t}$: braking and acceleration	**Discarded.** $\dot{v}_{x,t}$ as these signals are available at relatively low sampling rate, obtaining a reliable estimate is challenging
Lateral (y)	$\omega_{z,t} v_{x,t}$: centripetal during cornering	**Compensated.** $\omega_{z,t}$ from gyroscope; $v_{x,t}$ from CAN bus. Residual $\dot{v}_{y,t}$ is small and modelled.
Vertical (z)	$\omega_{x,t} v_{x,t}$: centripetal during pitching	**Compensated.** $\omega_{x,t}$ from gyroscope; $v_{x,t}$ from CAN bus. Residual $\dot{v}_{z,t}$ is small and modelled.

The residual lateral and vertical accelerations ($\dot{v}_{y,t}$ and $\dot{v}_{z,t}$) are modelled as first-order autoregressive processes:

$$\boldsymbol{\alpha}_t = c_a \, \boldsymbol{\alpha}_{t-1} + \boldsymbol{\varepsilon}_t, \qquad \boldsymbol{\alpha}_t = \begin{bmatrix} \alpha_{y,t} \\ \alpha_{z,t} \end{bmatrix}, \tag{4.23}$$

where $c_a = 0.90$ is the decay constant and $\boldsymbol{\varepsilon}_t$ is the model error. The estimate $\boldsymbol{\alpha}_t$ is updated at each step using a low-pass IIR smoother with rate $\lambda = 0.10$:

$$\boldsymbol{\alpha}_t \leftarrow (1-\lambda)\,\boldsymbol{\alpha}_{t-1} + \lambda\,\boldsymbol{\alpha}_t^{\mathrm{inst}}, \tag{4.24}$$

where $\boldsymbol{\alpha}_t^{\mathrm{inst}}$ is the instantaneous estimate computed from the current body-frame acceleration and velocity measurements. This IIR update decouples the alpha estimate from the current filter state, avoiding a circular dependency between the measurement residual and the correction term.
Dropping the negligible products $\omega_{y,t}v_{z,t}$ and $\omega_{y,t}v_{y,t}$, the compensated lateral and vertical accelerations become

$$a_{y,t} \approx c_a\,\alpha_{y,t-1} + \omega_{z,t}v_{x,t} + \varepsilon_{y,t}, \tag{4.25}$$

$$a_{z,t} \approx c_a\,\alpha_{z,t-1} - \omega_{x,t}v_{x,t} + \varepsilon_{z,t}. \tag{4.26}$$

Measurement Update 1: Lateral and Vertical Accelerometers

Substituting Equations (4.25)–(4.26) into the accelerometer measurement model and isolating the state-dependent component yields the corrected observation vector

$$\mathbf{z}_{t,1} = \mathbf{y}_{A,t,1} - c_a\,\boldsymbol{\alpha}_{t-1} - \mathbf{y}_{G,t,1}\,v_t, \tag{4.27}$$

where $\mathbf{y}_{A,t,1} = [y_{A,y},\ y_{A,z}]^T$ and $\mathbf{y}_{G,t,1} = [G_z,\ -G_x]^T$. This forms the standard linear measurement equation

$$\mathbf{z}_{t,1} = \mathbf{H}_1\,\mathbf{x}_t + \boldsymbol{\Upsilon}_{t,1}, \tag{4.28}$$

with measurement matrix

$$\mathbf{H}_1 = -g\begin{bmatrix}0 & 1 & 0\\ 0 & 0 & 1\end{bmatrix} = \begin{bmatrix}0 & -g & 0\\ 0 & 0 & -g\end{bmatrix}, \tag{4.29}$$

and combined measurement noise covariance

$$\mathbf{M}_{t,1} = \boldsymbol{\Sigma}_{\alpha_t} + \boldsymbol{\Sigma}_{GV} + \boldsymbol{\Sigma}_A, \tag{4.30}$$

where $\boldsymbol{\Sigma}_{GV} = \sigma_v^2\sigma_G^2\,\mathbf{I}_2 \approx 1.22\times10^{-9}\,\mathbf{I}_2$ accounts for noise from the speed–gyro product, $\boldsymbol{\Sigma}_A = \sigma_A^2\,\mathbf{I}_2 = 4\times10^{-4}\,\mathbf{I}_2$ is the accelerometer noise, and $\boldsymbol{\Sigma}_{\alpha_t} = \frac{1}{2}c_a^2\|\boldsymbol{\alpha}_{t-1}\|^2\,\mathbf{I}_2$ approximates the model error covariance following [20]. The Kalman update follows the standard form:

$$\mathbf{K}_{t,1} = \mathbf{P}_t^-\mathbf{H}_1^T\Big(\mathbf{H}_1\mathbf{P}_t^-\mathbf{H}_1^T + \mathbf{M}_{t,1}\Big)^{-1}, \tag{4.31}$$

$$\mathbf{x}_t^+ = \mathbf{x}_t^- + \mathbf{K}_{t,1}\Big(\mathbf{z}_{t,1} - \mathbf{H}_1\mathbf{x}_t^-\Big), \tag{4.32}$$

$$\mathbf{P}_t^+ = (\mathbf{I} - \mathbf{K}_{t,1}\mathbf{H}_1)\,\mathbf{P}_t^-. \tag{4.33}$$

After this update, the second and third state elements (corresponding to R_{32} and R_{33}) are corrected by the lateral and vertical accelerometer information. The first state element (R_{31}) remains uncorrected because the longitudinal accelerometer axis was discarded.

Measurement Update 2: Unit-Norm Constraint

Since $\mathbf{x}_t$ represents a unit-length gravity direction vector, its Euclidean norm is constrained to unity:

$$x_t(1)^2 + x_t(2)^2 + x_t(3)^2 = 1. \tag{4.34}$$

This constraint provides a second measurement that corrects the first state element without requiring the longitudinal accelerometer. Using the corrected second and third elements from Update 1:

$$z_{t,2} = \operatorname{sign}\Big(x_t^+(1)\Big)\sqrt{\max\Big(1 - x_t^+(2)^2 - x_t^+(3)^2,\ 0\Big)}, \tag{4.35}$$

which satisfies $z_{t,2} = x_t(1) + \delta_t$ with noise δ_t.

Remark. Although the square root in Equation (4.35) is nonlinear, the measurement equation itself is linear in $x_t(1)$: $z_{t,2} = \mathbf{H}_2\,\mathbf{x}_t + \delta_t$, with $\mathbf{H}_2 = \begin{bmatrix}1 & 0 & 0\end{bmatrix}$. No Extended Kalman Filter extension is therefore required.

The scalar measurement noise variance is $M_{t,2} = \mathbb{E}[\delta_t^2] = 1 \times 10^{-4}$. The Kalman equations for Update 2 follow the same standard form, applied to the post-Update-1 state and covariance $\mathbf{x}_t^+$ and $\mathbf{P}_t^+$. After both updates, the state is renormalised to unit length to prevent numerical drift:

$$\mathbf{x}_t^{++} \leftarrow \frac{\mathbf{x}_t^{++}}{\|\mathbf{x}_t^{++}\|}. \tag{4.36}$$

The complete single-iteration algorithm is summarised in Algorithm 1.

Algorithm 1: Two-stage attitude Kalman filter (one iteration)

Inputs: $\mathbf{x}_{t-1}^{++}$, $\mathbf{P}_{t-1}^{++}$, $\boldsymbol{\alpha}_{t-1}$; sensors $\mathbf{y}_A$, $\mathbf{y}_G$, v

1. Prediction: $\mathbf{x}_t^- = \boldsymbol{\Phi}_{t-1}\mathbf{x}_{t-1}^{++}$, $\mathbf{P}_t^- = \boldsymbol{\Phi}_{t-1}\mathbf{P}_{t-1}^{++}\boldsymbol{\Phi}_{t-1}^T + \mathbf{Q}_{t-1}$.

2. Update 1: form $\mathbf{z}_{t,1}$ via Eq. (4.27); compute $\mathbf{K}_{t,1}$, $\mathbf{x}_t^+$, $\mathbf{P}_t^+$.

3. Update 2: form $z_{t,2}$ via Eq. (4.35); compute $\mathbf{K}_{t,2}$, $\mathbf{x}_t^{++}$, $\mathbf{P}_t^{++}$.

4. Normalise: $\mathbf{x}_t^{++} \leftarrow \mathbf{x}_t^{++}/\|\mathbf{x}_t^{++}\|$.

5. Recover body acceleration: $\mathbf{a}_{\text{body},t} = \mathbf{y}_{A,t} + g\,\mathbf{x}_t^{++}$.

6. Update alpha (IIR): $\boldsymbol{\alpha}_t^{\text{inst}} = \mathbf{a}_{\text{body},t}[2{:}3] - v\,[\omega_z,\ -\omega_x]^T$; $\boldsymbol{\alpha}_t \leftarrow (1-\lambda)\boldsymbol{\alpha}_{t-1} + \lambda\boldsymbol{\alpha}_t^{\text{inst}}$.

Global Vertical Acceleration

Once the roll and pitch angles are estimated, the body-frame accelerations are projected onto the global vertical axis. The global vertical acceleration is computed as

$$\ddot{z}_{\text{IMU}} = \sin\theta\, a_x - \cos\theta\sin\phi\, a_y + \cos\theta\cos\phi\, a_z, \tag{4.37}$$

where a_x, a_y, and a_z are the gravity-compensated body-frame accelerations. A 0.05 Hz high-pass filter is subsequently applied to $\ddot{z}_{\mathrm{IMU}}$ to remove the residual low-frequency bias arising from imperfect gravity compensation (see Section 3.4). The resulting signal provides the IMU-based heave acceleration measurement used as input to the heave observer described in Section 4.3.
The complete sensor fusion architecture is illustrated in Figure 4.2.

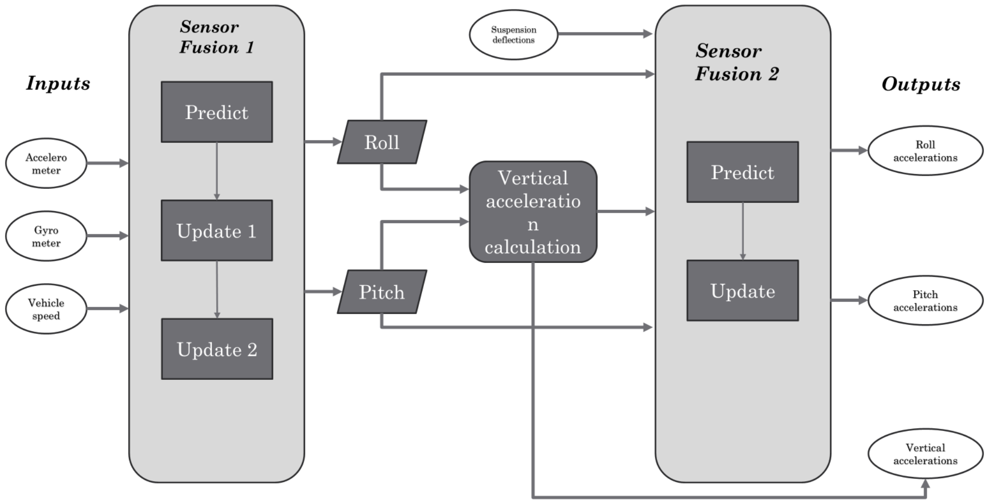

Figure 4.2: Sensor fusion architecture: accelerometer, gyroscope, and vehicle speed inputs are processed through the attitude Kalman filter to produce roll, pitch, and global vertical acceleration outputs.

4.3 Heave Observer

The heave observer estimates the vehicle body vertical acceleration by fusing two complementary signals: the global vertical acceleration $\ddot{z}_{\mathrm{IMU}}$ derived from the attitude estimator (Section 4.2), and a geometric heave displacement z_b reconstructed from the four suspension corner heights. The IMU signal provides high-frequency dynamic content with no low-frequency drift, while the suspension-derived measurement provides an independent low-frequency position reference. A Kalman filter is used to optimally combine these two complementary sources.

Geometric Heave from Suspension Deflections

The four suspension corner heights δ_{FL}, δ_{FR}, δ_{RL}, δ_{RR} are anti-aliasing filtered and resampled to the IMU time base. The geometric body heave is obtained from the corner-height average corrected for the estimated roll and pitch:

$$z_b = \frac{1}{4}\Big[(\delta_{FL}-l_f\theta-t_f\phi)+(\delta_{FR}-l_f\theta+t_f\phi)+(\delta_{RL}+l_r\theta-t_r\phi)+(\delta_{RR}+l_r\theta+t_r\phi)\Big], \quad (4.38)$$

using the vehicle geometry parameters $l_f = l_r =$ [redacted] m (CG-to-axle distance) and $t_f = t_r =$ [redacted] m (half-track width).

Heave Observer State Model

The observer uses a three-state kinematic model for vertical body motion:

$$\mathbf{x}_k = \begin{bmatrix} z_k \\ \dot{z}_k \\ \ddot{z}_k \end{bmatrix}, \tag{4.39}$$

where z_k, $\dot{z}_k$, and $\ddot{z}_k$ are the body heave position, velocity, and acceleration. The constant-acceleration discrete-time state transition is

$$\mathbf{x}_k = \mathbf{A}\,\mathbf{x}_{k-1} + \mathbf{w}_k, \qquad \mathbf{A} = \begin{bmatrix} 1 & \Delta t & \frac{1}{2}\Delta t^2 \\ 0 & 1 & \Delta t \\ 0 & 0 & 1 \end{bmatrix}. \tag{4.40}$$

The process noise is driven by vertical jerk, which represents unmodelled road excitation and changes in body acceleration:

$$\mathbf{Q}_k = \sigma_{j,k}^2\,\mathbf{G}\mathbf{G}^T, \qquad \mathbf{G} = \begin{bmatrix} \Delta t^3/6 \\ \Delta t^2/2 \\ \Delta t \end{bmatrix}. \tag{4.41}$$

The jerk standard deviation is speed-scaled to account for the increase in road excitation with vehicle speed:

$$\sigma_{j,k} = \sigma_j^* + 0.3\,v_k, \tag{4.42}$$

where σ_j^* is the optimised baseline value and v_k is the forward speed in m/s. This speed-scaling reflects the physical observation that road roughness excitation increases with vehicle speed. The filter is initialised with

$$\mathbf{P}_0 = \mathrm{diag}\Big[10^{-2},\ 10^{-2},\ 0.25\Big]\ \mathrm{m}^2,\ \mathrm{m}^2/\mathrm{s}^2,\ \mathrm{m}^2/\mathrm{s}^4. \tag{4.43}$$

Measurement Model and Pitch Gate

The observer fuses two measurements: the geometric heave position z_b and the IMU-derived vertical acceleration $\ddot{z}_{\mathrm{IMU}}$. The measurement vector and observation matrix are

$$\mathbf{y}_k = \begin{bmatrix} z_b(k) \\ \ddot{z}_{\mathrm{IMU}}(k) \end{bmatrix}, \qquad \mathbf{H} = \begin{bmatrix} 1 & 0 & 0 \\ 0 & 0 & 1 \end{bmatrix}. \tag{4.44}$$

The first row of $\mathbf{H}$ maps the suspension-derived position to the position state; the second row maps the IMU acceleration to the acceleration state. The velocity state is not directly observed. The measurement noise covariance is

$$\mathbf{R}_k = \begin{bmatrix} R_{zb,k} & 0 \\ 0 & R_{\ddot{z}} \end{bmatrix}, \tag{4.45}$$

where the IMU acceleration variance is fixed at $R_{\ddot{z}} = (0.03)^2 = 9 \times 10^{-4}\,\mathrm{m^2/s^4}$, and the suspension position variance is inflated by a pitch gate:

$$R_{zb,k} = \frac{R^*_{zb}}{\max(w_{\theta,k},\ 0.05)}. \tag{4.46}$$

When the pitch angle is small ($w_\theta \approx 1$), $R_{zb,k} \approx R^*_{zb}$ and the suspension measurement receives its nominal confidence. As pitch increases beyond 8°, w_θ decreases toward zero, inflating $R_{zb,k}$ and directing the filter to rely primarily on the IMU. This gate prevents the geometric heave estimate from being corrupted during heavy braking or strong pitch events. The optimised baseline parameters σ^*_j and R^*_{zb} are obtained from the grid-search procedure described in Section 5.1 and reported in Table 4.3.

Kalman Filter Implementation

At each time step the observer executes the standard predict–update cycle.

4.3.0.0.1 Prediction

$$\mathbf{x}^-_k = \mathbf{A}\,\mathbf{x}_{k-1}, \qquad \mathbf{P}^-_k = \mathbf{A}\,\mathbf{P}_{k-1}\,\mathbf{A}^T + \mathbf{Q}_k. \tag{4.47}$$

4.3.0.0.2 Update

$$\mathbf{K}_k = \mathbf{P}^-_k\mathbf{H}^T\Big(\mathbf{H}\mathbf{P}^-_k\mathbf{H}^T + \mathbf{R}_k\Big)^{-1}, \tag{4.48}$$

$$\mathbf{x}_k = \mathbf{x}^-_k + \mathbf{K}_k\Big(\mathbf{y}_k - \mathbf{H}\mathbf{x}^-_k\Big), \qquad \mathbf{P}_k = (\mathbf{I} - \mathbf{K}_k\mathbf{H})\,\mathbf{P}^-_k. \tag{4.49}$$

4.3.0.0.3 Output The heave acceleration estimate is the third component of the state vector:

$$\ddot{z}_{\mathrm{obs},k} = \hat{x}_{k,3}. \tag{4.50}$$

The output is band-pass filtered within the evaluation band (0.10–25 Hz) and time-aligned to the ground-truth reference using the peak cross-correlation lag prior to performance evaluation (Section 5.2).
Table 4.3 consolidates all heave observer design and tuning parameters.

Table 4.3: Summary of heave observer design and tuning parameters.

Parameter	Description	Value
σ^*_j (m/s^3)	Optimal baseline jerk noise std. (grid search)	0.667
R^*_{zb} (m^2)	Optimal suspension position variance	3.33×10^{-5}
$R_{\ddot{z}}$ (m^2/s^4)	IMU acceleration variance (fixed)	9.00×10^{-4}
$f_{\mathrm{HP,bias}}$ (Hz)	Bias-removal high-pass cut-off on $\ddot{z}_{\mathrm{IMU}}$	0.05
$f_{\mathrm{HP,eval}}$ (Hz)	Evaluation band lower limit	0.10
$f_{\mathrm{LP,eval}}$ (Hz)	Evaluation band upper limit	25.0
$l_f = l_r$ (m)	CG-to-axle distance	1.492
$t_f = t_r$ (m)	Half-track width	0.838

4.4 Roll and Pitch Observer

The roll and pitch observer estimates the vehicle body angular accelerations by fusing measurements from the SRS IMU and the four suspension deflection sensors. Although roll and pitch dynamics are mechanically coupled through the vehicle body, the two axes are estimated independently using identical Kalman filter structures. This parallel design is justified because the dominant dynamic characteristics of each axis can be captured without cross-axis coupling at the linear operating point, and it substantially reduces the complexity of the filter design and tuning. The complete signal-processing and estimation pipeline is described below.

Sensor Signals and Pre-Processing

IMU-Derived Angular Accelerations

The SRS IMU provides angular rate measurements p (roll rate) and q (pitch rate). Prior to differentiation, both signals are low-pass filtered at 25 Hz using a fourth-order Butterworth filter to suppress broadband sensor noise. An anti-aliasing cut-off is computed as

$$f_{\mathrm{aa}} = \min(0.45\,F_s,\ 0.45\,F_{s,\mathrm{corner}})\,, \tag{4.51}$$

where F_s is the IMU sampling frequency and $F_{s,\mathrm{corner}}$ is the suspension deflection sensor sampling frequency. This ensures that no aliasing is introduced when the suspension signals are resampled to the IMU time base. The IMU angular accelerations are obtained by differentiating the filtered angular rates using a Savitzky-Golay derivative filter (see Section 3.3), which provides noise-robust differentiation while preserving the shape of the derivative signal:

$$\ddot{\phi}_{\mathrm{IMU}} = \frac{dp}{dt}, \qquad \ddot{\theta}_{\mathrm{IMU}} = \frac{dq}{dt}. \tag{4.52}$$

Suspension-Based Roll and Pitch Angles

The four suspension deflection sensors provide corner height measurements δ_{FL}, δ_{FR}, δ_{RL}, δ_{RR}, where the subscripts denote front-left, front-right, rear-left, and rear-right respectively. The suspension signals are anti-aliasing filtered and resampled to the IMU time base using piecewise-cubic Hermite interpolation.
The vehicle is assumed to have symmetric axle geometry with parameters

$$l_f = l_r = \text{[redacted]}, \qquad t_f = t_r = \text{[redacted]}, \tag{4.53}$$

where l_f and l_r are the longitudinal distances from the centre of gravity to the front and rear axles, and t_f and t_r are the front and rear half-track widths. Under the small-angle approximation, the suspension-derived roll angle is obtained by averaging the lateral height asymmetry across both axles:

$$\phi_{\mathrm{susp}} = \frac{1}{2}\left[\frac{\delta_{FL} - \delta_{FR}}{2t_f} + \frac{\delta_{RL} - \delta_{RR}}{2t_r}\right], \tag{4.54}$$

and the suspension-derived pitch angle is obtained from the front-to-rear average height difference:

$$\theta_{\text{susp}} = \frac{\dfrac{\delta_{FL} + \delta_{FR}}{2} - \dfrac{\delta_{RL} + \delta_{RR}}{2}}{l_f + l_r}. \tag{4.55}$$

These geometric estimates are dominated by low-frequency body motion and serve as complementary inputs to the high-frequency-sensitive IMU. However, since suspension deflections also contain contributions from road irregularities and unsprung mass motion, they are not treated as pure body angle measurements and receive correspondingly low confidence in the filter.

Suspension-Derived Angular Accelerations

An additional, low-confidence angular acceleration measurement is obtained by twice differentiating the suspension angle signals. In discrete form:

$$\ddot{x}_k = \frac{x_k - 2x_{k-1} + x_{k-2}}{\Delta t^2}. \tag{4.56}$$

Double differentiation amplifies high-frequency noise quadratically with frequency. The resulting signals are therefore low-pass filtered at 8 Hz using a second-order Butterworth filter before use. This tighter cut-off, compared with the 25 Hz limit applied to the IMU rate channels, is necessary to suppress the noise floor that would otherwise dominate the roll acceleration estimates. The resulting signals capture only the low-frequency body-motion content and are used solely as weak corrective inputs in the measurement update.

Observer State Model

The same constant-angular-acceleration kinematic model is applied independently to both axes. For roll, the state vector is

$$\mathbf{x}_{\phi,k} = \begin{bmatrix} \phi_k \\ \dot{\phi}_k \\ \ddot{\phi}_k \end{bmatrix}, \tag{4.57}$$

where ϕ_k, $\dot{\phi}_k$, and $\ddot{\phi}_k$ are the roll angle, angular rate, and angular acceleration at time step k. An identical structure applies to pitch:

$$\mathbf{x}_{\theta,k} = \begin{bmatrix} \theta_k \\ \dot{\theta}_k \\ \ddot{\theta}_k \end{bmatrix}. \tag{4.58}$$

The discrete-time state transition model is

$$\mathbf{x}_k = \mathbf{A}\,\mathbf{x}_{k-1} + \mathbf{w}_k, \qquad \mathbf{A} = \begin{bmatrix} 1 & \Delta t & \frac{1}{2}\Delta t^2 \\ 0 & 1 & \Delta t \\ 0 & 0 & 1 \end{bmatrix}. \tag{4.59}$$

This model propagates the current angular acceleration as constant over the interval Δt, with angular jerk acting as the stochastic driving input. The process noise covariance is parameterised by the angular jerk standard deviation σ_j:

$$\mathbf{Q} = \sigma_j^2 \, \mathbf{G}\mathbf{G}^T, \qquad \mathbf{G} = \begin{bmatrix} \Delta t^3/6 \\ \Delta t^2/2 \\ \Delta t \end{bmatrix}. \tag{4.60}$$

The parameter σ_j controls the filter's agility in tracking rapid changes in angular acceleration and is determined independently for each axis through the grid-search optimisation described in Section 5.1, yielding

$$\sigma_{j,\phi}^* = 0.692 \text{ rad/s}^3 \quad \text{(roll)}, \qquad \sigma_{j,\theta}^* = 0.998 \text{ rad/s}^3 \quad \text{(pitch)}. \tag{4.61}$$

The filter is initialised with $\hat{\mathbf{x}}_0 = [\phi_{\text{susp}}(1),\ p_{\text{IMU}}(1),\ \ddot{\phi}_{\text{IMU}}(1)]^T$ (and the pitch equivalent), and initial error covariance

$$\mathbf{P}_0 = \text{diag}\left[\left(\tfrac{\pi}{180}\right)^2,\ \left(\tfrac{\pi}{180}\right)^2,\ \left(\tfrac{5\pi}{180}\right)^2\right] \ \text{rad}^2,\ \text{rad}^2/\text{s}^2,\ \text{rad}^2/\text{s}^4, \tag{4.62}$$

reflecting moderate a priori uncertainty in angle ($\pm 1°$) and angular rate ($\pm 1°$/s), and larger uncertainty in the initial angular acceleration ($\pm 5°/\text{s}^2$).

Measurement Model

Each observer fuses four measurement signals: the suspension-derived body angle, the IMU angular rate, the IMU-derived angular acceleration, and the suspension-derived angular acceleration. For roll, the measurement vector is

$$\mathbf{y}_{\phi,k} = \begin{bmatrix} \phi_{\text{susp},k} \\ p_{\text{IMU},k} \\ \ddot{\phi}_{\text{IMU},k} \\ \ddot{\phi}_{\text{susp},k} \end{bmatrix}, \qquad \mathbf{y}_{\theta,k} = \begin{bmatrix} \theta_{\text{susp},k} \\ q_{\text{IMU},k} \\ \ddot{\theta}_{\text{IMU},k} \\ \ddot{\theta}_{\text{susp},k} \end{bmatrix}. \tag{4.63}$$

The measurement matrix is identical for both axes:

$$\mathbf{H} = \begin{bmatrix} 1 & 0 & 0 \\ 0 & 1 & 0 \\ 0 & 0 & 1 \\ 0 & 0 & 1 \end{bmatrix}. \tag{4.64}$$

The first row maps the suspension angle to the angle state; the second maps the IMU rate to the rate state; and the third and fourth rows both project onto the angular acceleration state, enabling the filter to fuse the two independent acceleration sources in a single update step. The measurement noise covariance matrix is diagonal:

$$\mathbf{R} = \text{diag}\left[R_{\text{susp}},\ R_{\dot{\phi}},\ R_{\ddot{\phi},\text{IMU}},\ R_{\ddot{\phi},\text{susp}}\right]. \tag{4.65}$$

The three fixed entries, held constant for both axes, are set from sensor specifications and signal-processing considerations:

$$R_{\dot{\phi}} = \left(\tfrac{0.03\pi}{180}\right)^2 \approx 2.74 \times 10^{-7}\ \mathrm{rad}^2/\mathrm{s}^2, \tag{4.66}$$

$$R_{\ddot{\phi},\mathrm{IMU}} = \left(\tfrac{0.5\pi}{180}\right)^2 \approx 7.62 \times 10^{-5}\ \mathrm{rad}^2/\mathrm{s}^4, \tag{4.67}$$

$$R_{\ddot{\phi},\mathrm{susp}} = \left(\tfrac{50\pi}{180}\right)^2 \approx 0.762\ \mathrm{rad}^2/\mathrm{s}^4. \tag{4.68}$$

The large variance assigned to the suspension-derived angular acceleration reflects the substantial noise amplification introduced by double differentiation. This entry is three to four orders of magnitude larger than the IMU acceleration variance, ensuring that the suspension-derived acceleration contributes only a weak low-frequency correction while the IMU dominates the update.
The suspension angle variance R_{susp} is the primary tuning parameter, optimised independently for each axis via grid search:

$$R^*_{\mathrm{susp},\phi} = 9.14 \times 10^{-2}\ \mathrm{rad}^2 \quad \text{(roll)}, \qquad R^*_{\mathrm{susp},\theta} = 1.02 \times 10^{-6}\ \mathrm{rad}^2 \quad \text{(pitch)}. \tag{4.69}$$

The five-orders-of-magnitude disparity between these values reflects the fundamentally different quality of the suspension-derived angle in each axis. For pitch, the front-to-rear height difference is a clean, high-SNR measurement of the dominant body pitching motion, and the filter assigns it near-full confidence. For roll, the lateral height asymmetry is strongly contaminated by road cross-slope inputs and unsprung mass dynamics, so the filter is directed to rely far more heavily on the process model and the IMU rate signal.

Kalman Filter Implementation

At each discrete time step k, the observer executes the standard linear Kalman filter predict–update cycle identically for both axes.

4.4.0.0.1 Prediction

$$\hat{\mathbf{x}}_k^- = \mathbf{A}\,\hat{\mathbf{x}}_{k-1}, \qquad \mathbf{P}_k^- = \mathbf{A}\,\mathbf{P}_{k-1}\,\mathbf{A}^T + \mathbf{Q}. \tag{4.70}$$

4.4.0.0.2 Update

$$\mathbf{K}_k = \mathbf{P}_k^-\mathbf{H}^T\left(\mathbf{H}\,\mathbf{P}_k^-\mathbf{H}^T + \mathbf{R}\right)^{-1}, \tag{4.71}$$

$$\hat{\mathbf{x}}_k = \hat{\mathbf{x}}_k^- + \mathbf{K}_k\Big(\mathbf{y}_k - \mathbf{H}\,\hat{\mathbf{x}}_k^-\Big), \qquad \mathbf{P}_k = (\mathbf{I} - \mathbf{K}_k\mathbf{H})\,\mathbf{P}_k^-. \tag{4.72}$$

4.4.0.0.3 Output The angular acceleration estimates are extracted as the third component of each state vector:

$$\ddot{\phi}_{\mathrm{obs}} = \hat{x}_{\phi,3}, \qquad \ddot{\theta}_{\mathrm{obs}} = \hat{x}_{\theta,3}. \tag{4.73}$$

These signals are band-pass filtered within the respective evaluation bands (0.1–8 Hz for roll, 0.1–10 Hz for pitch) and time-aligned to the ground-truth reference

Algorithm 2: Roll and Pitch Observer (one iteration, applied independently to each axis)

Inputs (roll): $\hat{\mathbf{x}}_{\phi,k-1},\ \mathbf{P}_{\phi,k-1},\ p_{\mathrm{IMU},k},\ \ddot{\phi}_{\mathrm{IMU},k},\ \phi_{\mathrm{susp},k},\ \ddot{\phi}_{\mathrm{susp},k}$
Inputs (pitch): $\hat{\mathbf{x}}_{\theta,k-1},\ \mathbf{P}_{\theta,k-1},\ q_{\mathrm{IMU},k},\ \ddot{\theta}_{\mathrm{IMU},k},\ \theta_{\mathrm{susp},k},\ \ddot{\theta}_{\mathrm{susp},k}$

Pre-processing (performed before each iteration):

1. Low-pass filter IMU angular rates at 25 Hz (4th-order Butterworth): $p_f \leftarrow \mathrm{LPF}_{25}(p),\ q_f \leftarrow \mathrm{LPF}_{25}(q)$.

2. Differentiate filtered rates via Savitzky–Golay filter: $\ddot{\phi}_{\mathrm{IMU}} = dp_f/dt$, $\ddot{\theta}_{\mathrm{IMU}} = dq_f/dt$.

3. Compute suspension angles via Eq. (4.54)–(4.55); resample to IMU time base.

4. Compute suspension angular accelerations via Eq. (4.56); low-pass filter at 8 Hz.

For each axis $\star \in \{\phi,\, \theta\}$:

5. Assemble measurement vector:

$$\mathbf{y}_{\star,k} = \begin{bmatrix} \star_{\mathrm{susp},k} & \dot{\star}_{\mathrm{IMU},k} & \ddot{\star}_{\mathrm{IMU},k} & \ddot{\star}_{\mathrm{susp},k} \end{bmatrix}^T$$

6. Prediction step:

$$\hat{\mathbf{x}}^-_{\star,k} = \mathbf{A}\,\hat{\mathbf{x}}_{\star,k-1}$$
$$\mathbf{P}^-_{\star,k} = \mathbf{A}\,\mathbf{P}_{\star,k-1}\,\mathbf{A}^T + \mathbf{Q}_\star$$

7. Kalman gain:

$$\mathbf{K}_{\star,k} = \mathbf{P}^-_{\star,k}\mathbf{H}^T\Big(\mathbf{H}\,\mathbf{P}^-_{\star,k}\mathbf{H}^T + \mathbf{R}_\star\Big)^{-1}$$

8. Update step:

$$\hat{\mathbf{x}}_{\star,k} = \hat{\mathbf{x}}^-_{\star,k} + \mathbf{K}_{\star,k}\Big(\mathbf{y}_{\star,k} - \mathbf{H}\,\hat{\mathbf{x}}^-_{\star,k}\Big)$$
$$\mathbf{P}_{\star,k} = (\mathbf{I} - \mathbf{K}_{\star,k}\mathbf{H})\,\mathbf{P}^-_{\star,k}$$

9. Extract output:

$$\ddot{\phi}_{\mathrm{obs},k} = \hat{x}_{\phi,k,3} \qquad \ddot{\theta}_{\mathrm{obs},k} = \hat{x}_{\theta,k,3}$$

10. Band-pass filter outputs within evaluation bands:
Roll: 0.1–8 Hz Pitch: 0.1–10 Hz

Table 4.4: Summary of roll and pitch observer design and tuning parameters.

Parameter	**Description**	**Roll**	**Pitch**
σ_j^* (rad/s^3)	Optimal process noise (angular jerk std.)	0.6922	0.9977
R^*_{susp} (rad^2)	Optimal suspension angle variance	9.14×10^{-2}	1.02×10^{-6}
$R_{\dot\phi}$ (rad^2/s^2)	IMU angular rate variance (fixed)	2.74×10^{-7}	
$R_{\ddot\phi,\text{IMU}}$ (rad^2/s^4)	IMU angular acceleration variance (fixed)	7.62×10^{-5}	
$R_{\ddot\phi,\text{susp}}$ (rad^2/s^4)	Suspension angular acceleration variance (fixed)	7.62×10^{-1}	
$f_{\text{LP,IMU}}$ (Hz)	IMU angular rate low-pass cut-off	25	
$f_{\text{LP,susp}}$ (Hz)	Suspension acceleration low-pass cut-off	8	
$t_f = t_r$ (m)	Half-track width	0.838	
$l_f = l_r$ (m)	CG-to-axle distance	1.492	
Eval. band (Hz)	Frequency range for performance evaluation	0.1–8.0	0.1–10.0

using the peak cross-correlation lag prior to performance evaluation (Section 5.4 and Section 5.3).

Table 4.4 consolidates all observer parameters for both axes.

5
Results and Performance Evaluation

This chapter presents the performance evaluation of the proposed sensor-fusion observer framework for estimating vehicle body accelerations. The evaluation is based on vehicle measurement data provided by Volvo Cars, recorded at the Hällered Proving Ground under representative real-world driving conditions.

The observer outputs for heave, roll, and pitch accelerations are assessed against ground-truth signals derived from the dedicated onboard accelerometer system. A synchronisation correction of $\Delta t_{\text{sync}} = 0.020\,\text{s}$ was applied to all channels prior to evaluation using the peak cross-correlation lag. Performance is characterised through a combination of time-domain metrics (RMSE, normalised RMSE, Pearson correlation, phase lag), frequency-domain metrics (power spectral density, mean squared coherence, mean normalised error power), and the ISO 2631-1 perceptually weighted error, which concentrates evaluation on the frequency bands most relevant to human ride comfort perception [24].

The chapter is structured as follows: Section 5.1 describes the tuning methodology and cost function common to all three observers; Sections 5.2–5.4 present the individual tuning results and performance evaluations; and Section 5.5 provides a unified comparative discussion and directly addresses the central research question of this thesis.

5.1 Observer Tuning Methodology

A consistent tuning strategy was applied to all three observers. For each axis, a systematic two-stage grid-search optimisation was performed over two Kalman filter parameters: the process noise standard deviation σ_j, representing the uncertainty in the jerk dynamics, and the suspension-derived measurement variance R_{susp} (or R_{zb} for heave), representing the confidence assigned to the geometric suspension measurements. A coarse sweep over a broad parameter space was first conducted to locate the approximate global minimum, followed by a fine search in the neighbourhood of the coarse optimum to obtain the final tuning configuration.

The optimisation objective was formulated as a composite cost function that balances amplitude accuracy, waveform similarity, phase fidelity, and spectral performance:

$$J = w_1\,\text{NRMSE} + w_2\,(1 - r) + w_3\,\text{NPLR} + w_4\,\text{NEC}_{\text{lin}}, \tag{5.1}$$

where r is the Pearson correlation coefficient (waveform shape similarity), NRMSE is the normalised root-mean-square error (amplitude accuracy), NPLR is the ground-truth-power-weighted mean absolute phase angle normalised by π (phase fidelity across the evaluation band), and $\mathrm{NEC}_{\mathrm{lin}}$ is the mean fractional error power spectral density within the evaluation band (spectral accuracy). All four terms are dimensionless and bounded in [0, 1], so the cost J is also bounded in [0, 1], with lower values indicating better performance. The baseline weighting vector used for all observers was

$$[w_1,\ w_2,\ w_3,\ w_4] = [0.35,\ 0.25,\ 0.25,\ 0.15]. \tag{5.2}$$

The highest weight is assigned to NRMSE ($w_1 = 0.35$) because amplitude accuracy is the most direct measure of whether the observer output could substitute for a dedicated accelerometer signal in a downstream suspension controller, a signal with the correct waveform shape but wrong amplitude would produce incorrect actuator commands. The correlation and phase terms receive equal intermediate weights ($w_2 = w_3 = 0.25$), reflecting the importance of both timing fidelity and waveform tracking for dynamic control applications, where a phase-shifted estimate can be more harmful than a slightly noisy one. The spectral term receives the lowest weight ($w_4 = 0.15$) because it is partially redundant with NRMSE and correlation in the primary ride band, and penalising high-frequency spectral mismatch too heavily would bias the optimisation toward over-smoothed estimates that look clean in the frequency domain but miss transient events in the time domain.

In addition to the composite cost, observer accuracy was assessed using the ISO 2631-1 frequency-weighting filters [24]: W_k for heave and W_e/W_d for pitch and roll. Broadband metrics such as NRMSE weight all frequencies equally, which can be misleading for suspension control applications where most energy lies in the 1–25 Hz primary ride band. The ISO filters emphasise precisely the frequency bands to which the human body is most sensitive, making the ISO-weighted error the most practically relevant single metric for assessing ride-comfort impact. It therefore serves as a perceptually motivated complement to the broadband error metrics throughout this chapter.

5.2 Heave Observer: Tuning and Performance

5.2.1 Tuning and Optimisation

The heave observer was tuned by optimising σ_j and the suspension-derived heave measurement variance R_{zb} over the evaluation dataset. The optimisation converged to a well-defined minimum, and a sensitivity analysis confirmed that the optimal parameter values remained invariant across five different weighting configurations of the cost function. This invariance demonstrates that the identified optimum reflects a physically meaningful and robust configuration rather than an artefact of a particular weighting choice.

The relatively low value of $\sigma_j = 0.667\,\mathrm{m/s^3}$ indicates that a smooth jerk process model is most appropriate for heave estimation, consistent with the predomi-

nantly low-frequency character of vertical body motion. The small value of $R_{zb} = 3.33 \times 10^{-5}\,\mathrm{m}^2$ reflects the high confidence assigned to the suspension-derived heave position within the filter.
The coarse and fine optimisation landscapes are shown in Figures 5.1 and 5.2 respectively, and the one-dimensional cost sensitivity around the optimum is illustrated in Figure 5.3.

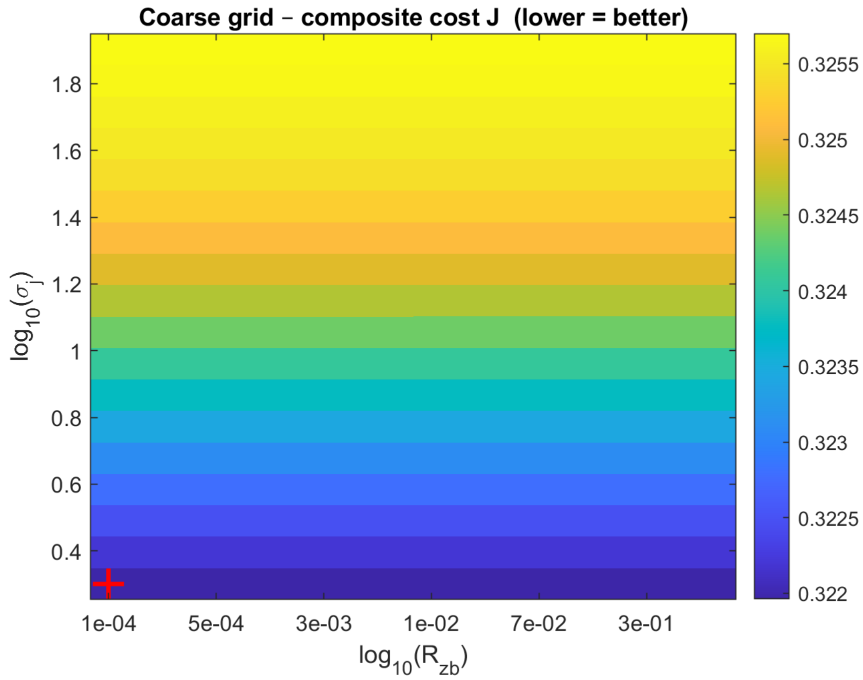

Figure 5.1: Coarse grid-search cost surface for the heave observer. The marker indicates the identified coarse optimum.

5.2.2 Performance Evaluation

Following optimisation, the heave observer was evaluated over the frequency band 0.10–20.0 Hz. The full set of performance metrics is reported in Table 5.1.
The time-domain comparison shown in Figure 5.4 demonstrates that the observer closely follows the dominant oscillatory characteristics of the reference heave acceleration throughout the evaluation interval. The Pearson correlation of 0.854 and the envelope correlation of 0.865 confirm strong agreement in both instantaneous waveform shape and amplitude modulation. The RMSE of $0.152\,\mathrm{m/s}^2$ and NRMSE of 0.521 indicate a moderate absolute error relative to the signal amplitude, with residual discrepancies attributable primarily to high-frequency transient events that fall outside the primary ride band.
The frequency-domain results in Figure 5.5 show that the observer reproduces the spectral content of the reference signal with reasonable fidelity across the primary ride region. The mean NEC of $-3.37\,\mathrm{dB}$ confirms that the observer error power remains below the signal power on average. At frequencies above approximately 10 Hz, a progressive reduction in estimated spectral energy is observed, consistent

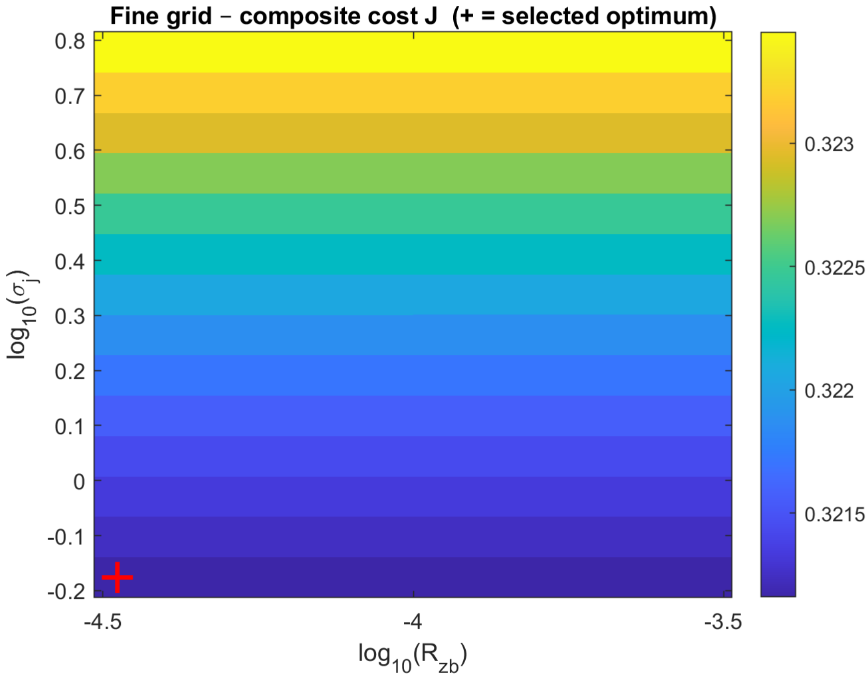

Figure 5.2: Fine grid-search cost surface for the heave observer, zoomed into the neighbourhood of the coarse optimum. The marker indicates the final selected parameter combination.

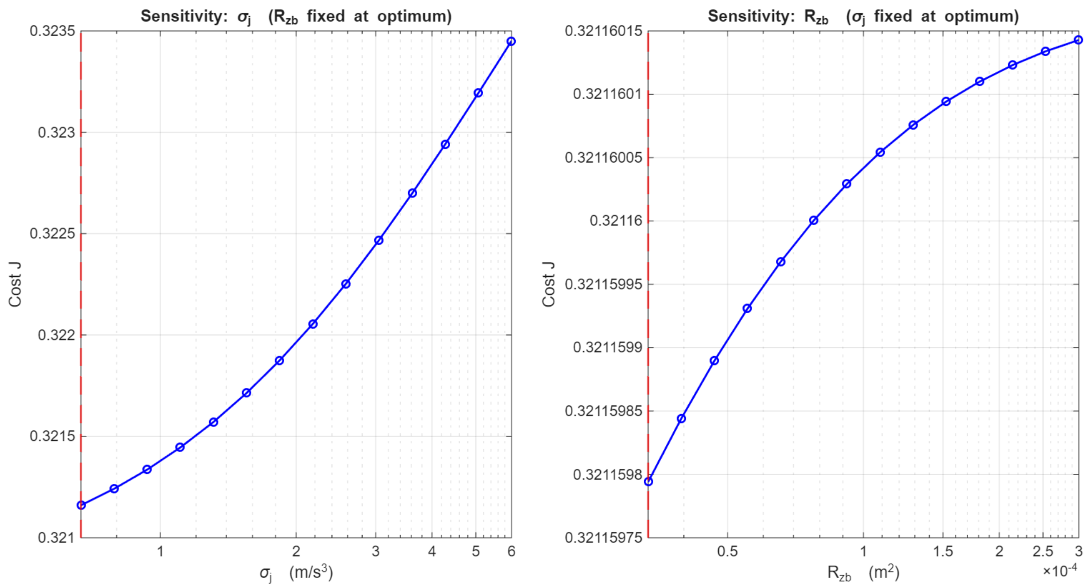

Figure 5.3: One-dimensional cost sensitivity with respect to σ_j (left) and R_{zb} (right) around the heave observer optimum.

Table 5.1: Performance metrics for the heave acceleration observer. Evaluation band: 0.10–20.0 Hz.

Metric	Unit	Value	Notes
RMSE	m/s^2	0.1516	Absolute amplitude error
NRMSE	–	0.5214	52% of ground-truth RMS
Pearson correlation (r)	–	0.8544	Strong waveform tracking
Mean phase lag	deg	12.89	≈36 ms at 1 Hz
ISO 2631-1 W_k error	m/s^2	0.0899	Ground-truth W_k RMS = 0.2111
Mean coherence ($\bar{\gamma}^2$)	–	0.554	Above 0.5 threshold
Envelope correlation	–	0.8651	Hilbert amplitude
Mean NEC	dB	-3.37	Error power below signal power
Synchronisation lag	s	0.020	Removed by cross-correlation
Tuned σ_j^*	m/s^3	0.667	Speed-scaled in observer
Tuned R_{zb}^*	m^2	3.33×10^{-5}	Pitch-gated in observer

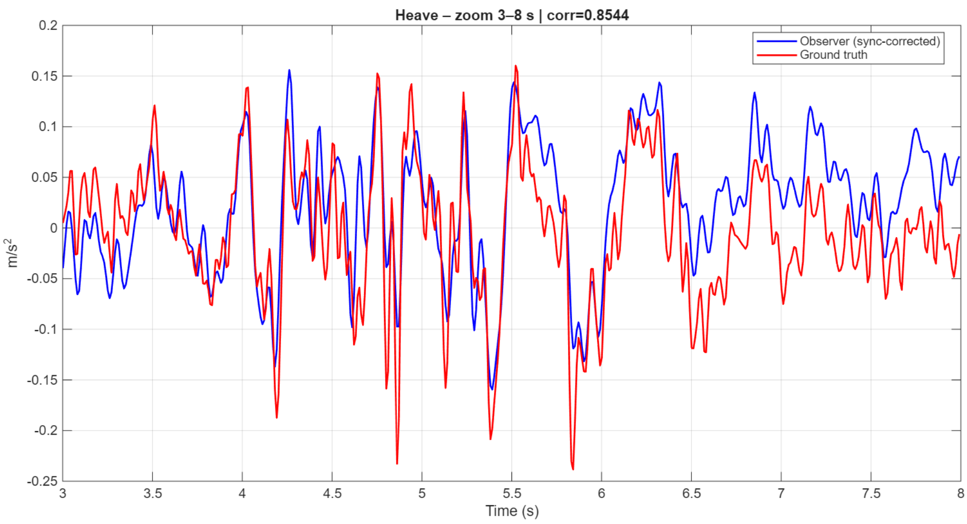

Figure 5.4: Time-domain comparison between the estimated and reference heave acceleration signals.

with the low-pass characteristics introduced by the linear process model and the filter's noise-suppression strategy.

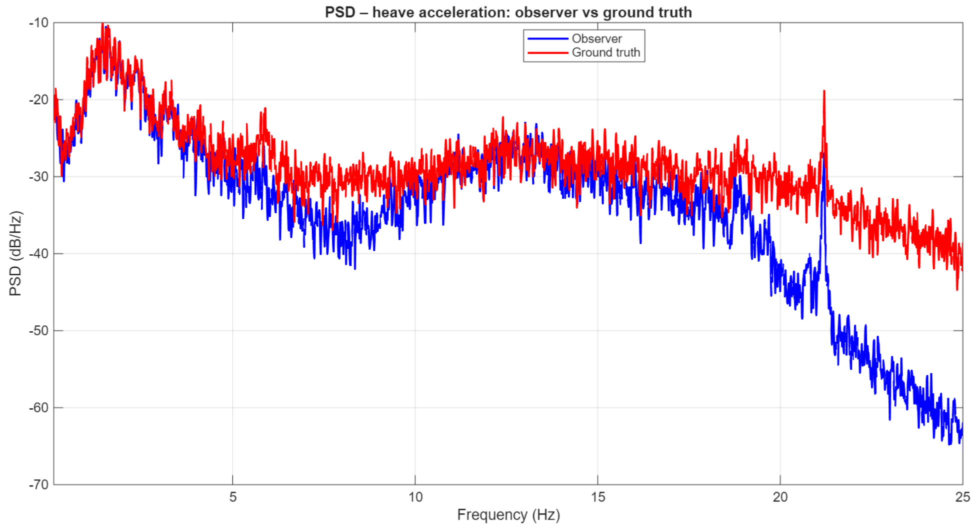

Figure 5.5: Power spectral density comparison between the heave observer output and the reference signal.

From a ride-comfort perspective, the ISO 2631-1 W_k-weighted error of $0.0899\,\mathrm{m/s^2}$ is substantially lower than the broadband NRMSE would suggest, representing 43% of the ground-truth W_k RMS of $0.2111\,\mathrm{m/s^2}$. This indicates that most estimation inaccuracies occur outside the frequency range most perceptually significant to vehicle occupants. Taken together, the heave results support a qualified positive answer to the central research question: the SRS-based observer can reproduce heave acceleration to a standard sufficient for ride-comfort assessment, with strongest fidelity in the 1–10 Hz primary ride band. The envelope comparison in Figure 5.6 further confirms consistent vibration intensity tracking over time.

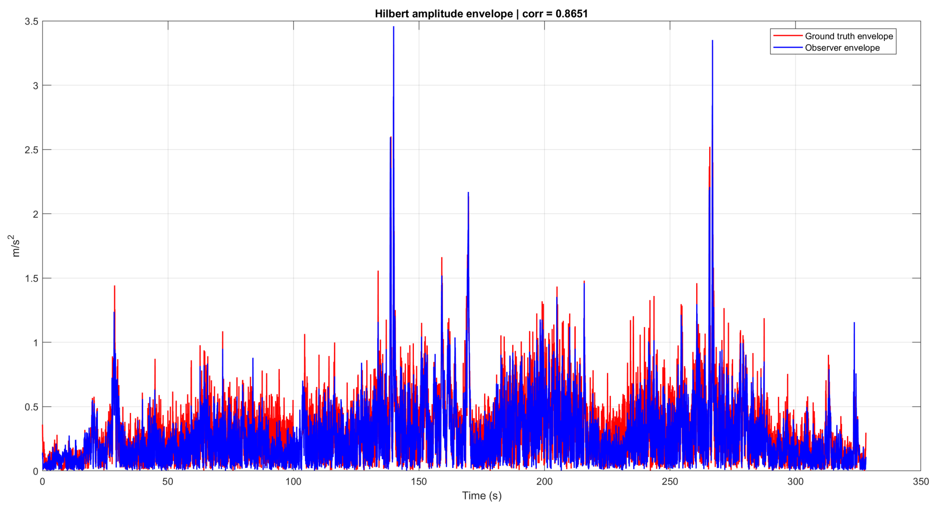

Figure 5.6: Comparison of the Hilbert envelopes of the estimated and reference heave acceleration signals, confirming consistent vibration intensity tracking over the evaluation interval.

5.3 Pitch Observer: Tuning and Performance

5.3.1 Tuning and Optimisation

The pitch observer was tuned using the same two-stage grid-search procedure, optimising σ_j and the suspension-derived pitch measurement variance R_{susp}. The optimisation converged to an extremely small measurement variance of $R_{\text{susp}} = 1.02 \times 10^{-6}\,\text{rad}^2$, indicating that the suspension-derived pitch angle provides highly informative and consistent observations. Consequently, the Kalman filter assigns a substantially higher weighting to the measurement update stage compared with the heave and roll observers. The process noise of $\sigma_j = 0.998\,\text{rad/s}^3$ reflects a moderately dynamic angular jerk assumption.

The optimisation landscape, shown in Figures 5.8 and 5.9, exhibits a sharp and well-defined minimum, confirming a unique and physically meaningful tuning solution.

5.3.2 Performance Evaluation

The pitch observer was evaluated over the frequency band 0.1–10 Hz. The performance metrics are reported in Table 5.2 alongside those of the roll observer, and demonstrate excellent agreement with the ground-truth angular acceleration signal.

The time-domain comparison in Figure 5.10 shows that the observer accurately tracks both the phase and amplitude of the dominant pitch dynamics across the evaluation interval. The Pearson correlation of 0.953 and envelope correlation of 0.942 indicate near-exact waveform reproduction, while the low NRMSE of 0.302 confirms a small relative amplitude error. The mean phase lag of only 3.5° demonstrates highly responsive dynamic tracking with negligible estimation delay.

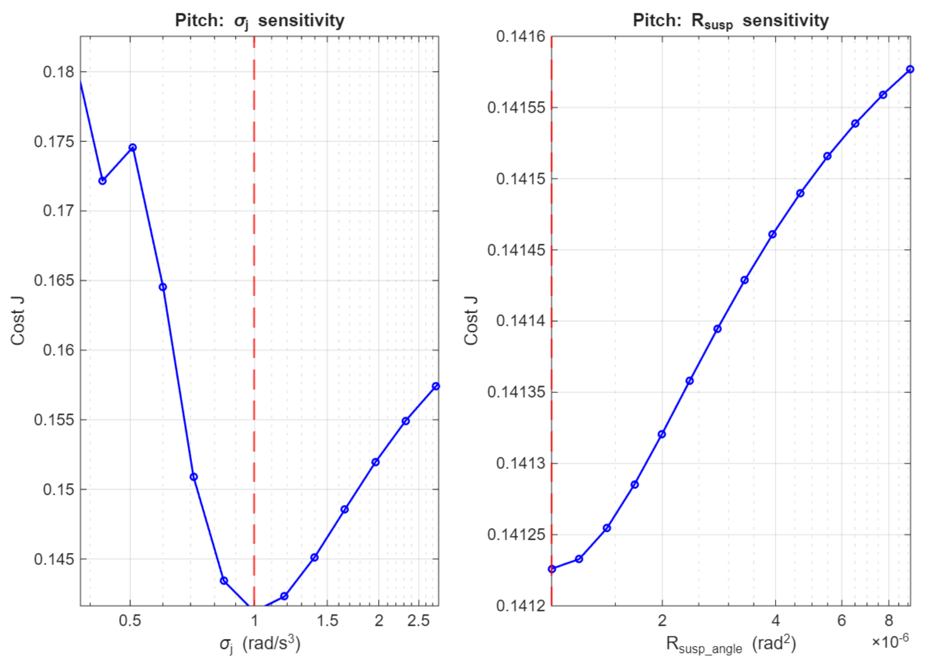

Figure 5.7: One-dimensional cost slices through the optimal pitch observer tuning, showing the sensitivity of the cost function to σ_j (left) and R_{susp} (right).

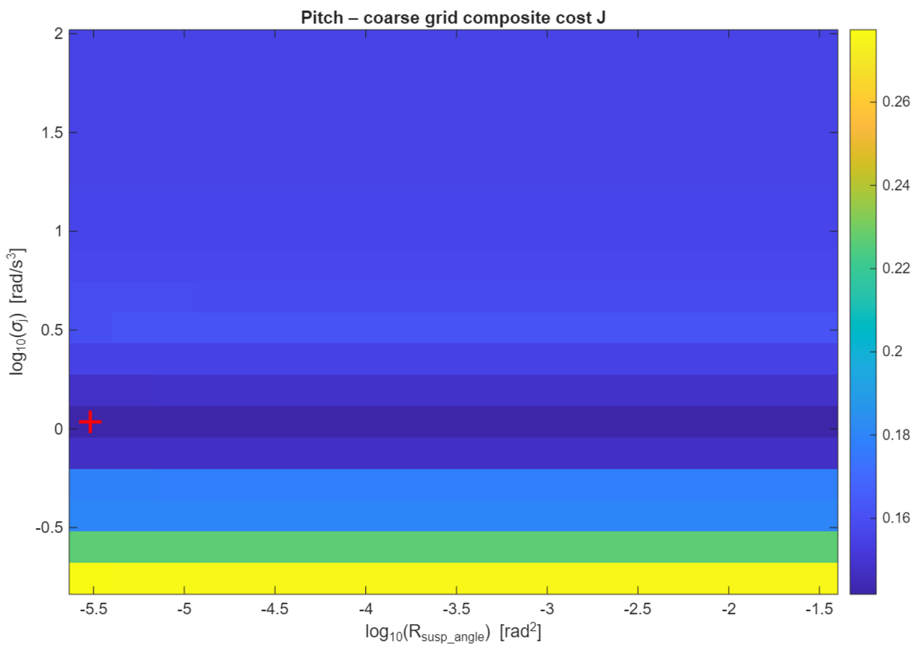

Figure 5.8: Coarse grid-search cost surface for the pitch observer. The marker indicates the identified optimal parameter combination.

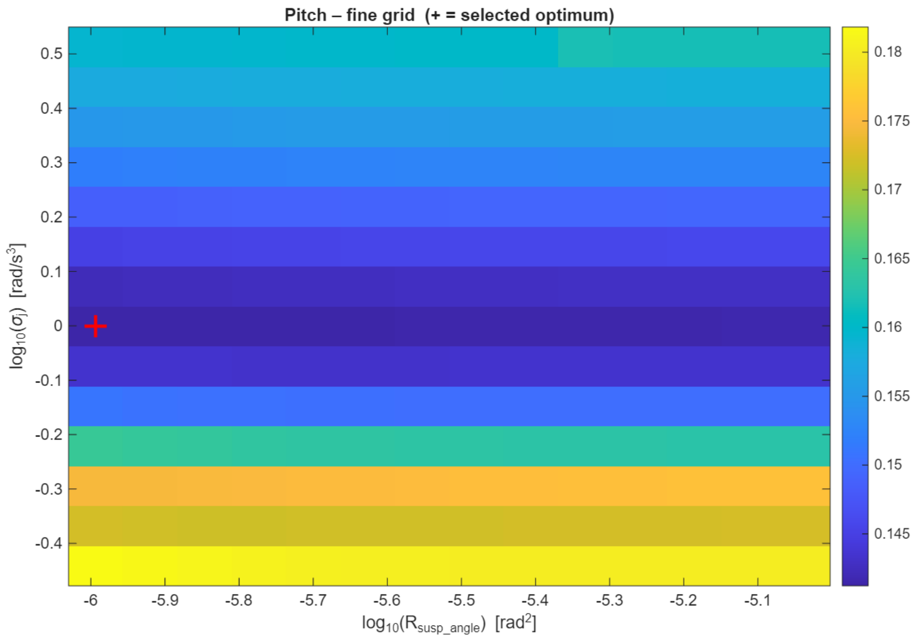

Figure 5.9: Fine grid-search cost surface for the pitch observer, zoomed into the neighbourhood of the coarse optimum. The marker indicates the final selected parameter combination.

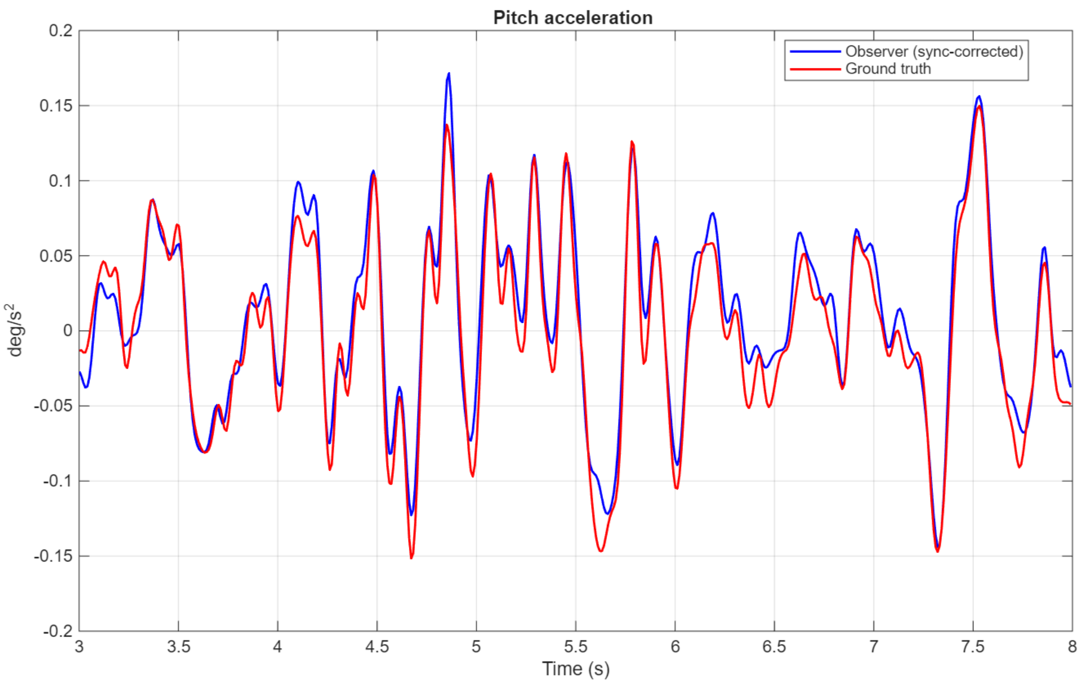

Figure 5.10: Time-domain comparison between the estimated and reference pitch angular acceleration signals.

The frequency-domain results in Figure 5.11 confirm strong spectral agreement across the primary pitch dynamics band. The mean coherence of 0.889 indicates a strong linear relationship between the estimated and reference signals, and the mean NEC of $-10.18\,\mathrm{dB}$ confirms that the estimation error power remains substantially below the signal power throughout the evaluation band. The ISO-weighted error of $0.0330\,\mathrm{deg/s^2}$ further demonstrates that observer inaccuracies are concentrated outside the perceptually critical frequency range.

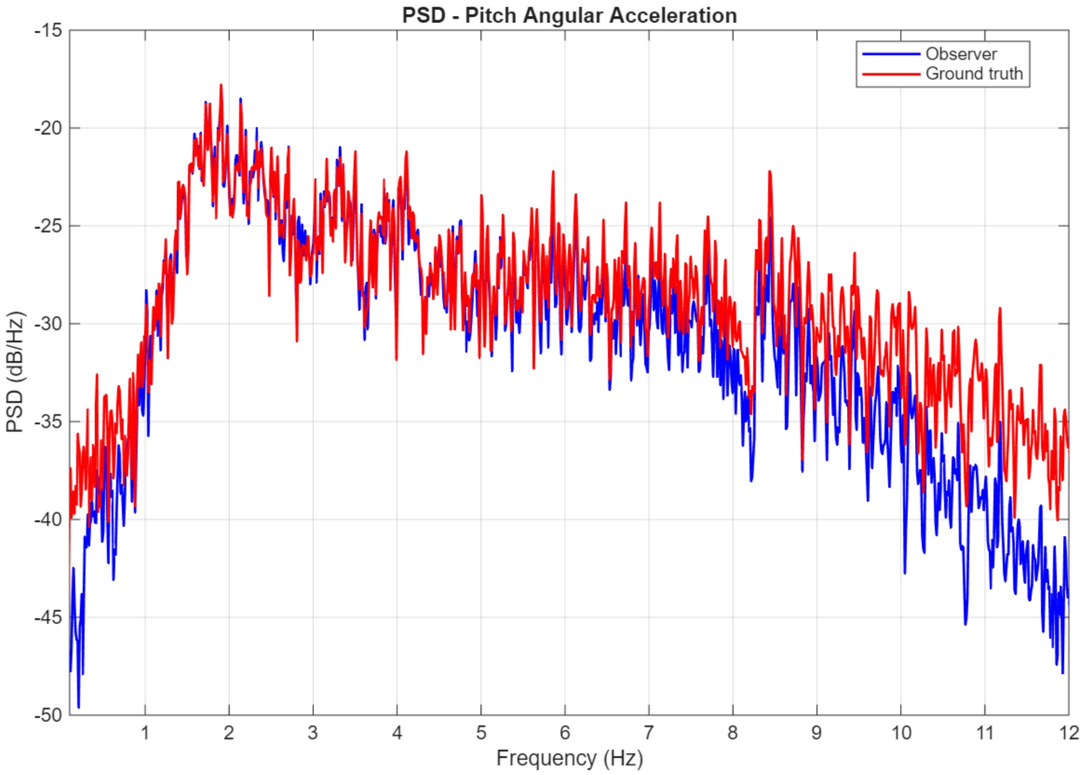

Figure 5.11: Power spectral density comparison between the estimated and reference pitch angular acceleration signals.

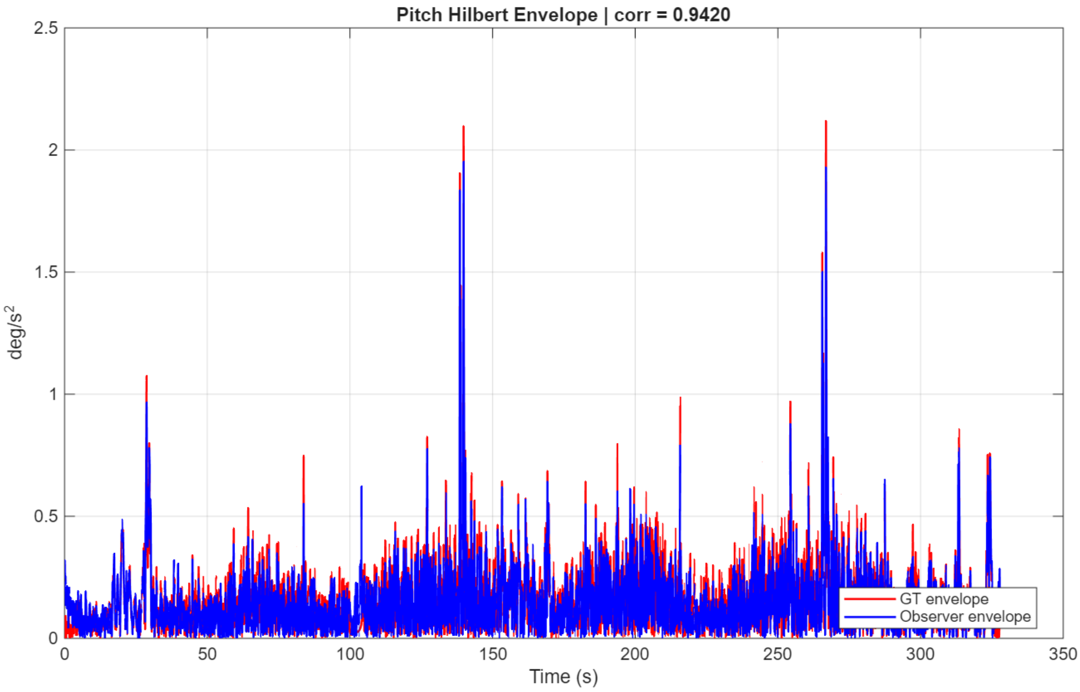

Figure 5.12: Comparison of the Hilbert envelopes of the estimated and reference pitch angular acceleration signals.

5.4 Roll Observer: Tuning and Performance

5.4.1 Tuning and Optimisation

The roll observer was tuned using the same grid-search methodology. In contrast to the pitch observer, the optimisation converged to a large measurement variance of $R_{\text{susp}} = 9.14 \times 10^{-2}\,\text{rad}^2$, indicating that the filter relies more heavily on the process model and inertial measurements than on the suspension-derived roll angle. This reflects the inherently lower signal-to-noise ratio and greater nonlinear content of the roll dynamics compared with pitch and heave. The optimal process noise of $\sigma_j = 0.692\,\text{rad/s}^3$ is consistent with a moderately smooth angular jerk assumption.
The optimisation landscape in Figures 5.14 and 5.15 shows a broader and shallower minimum compared with the pitch observer, consistent with the reduced observability of the roll dynamics and the lower information content of the suspension-derived roll angle.

5.4.2 Performance Evaluation

The roll observer was evaluated over the frequency band 0.1–8 Hz. As summarised in Table 5.2, the roll observer achieves more moderate performance than the pitch and heave observers across all metrics.
The time-domain comparison in Figure 5.16 shows that the observer captures the dominant low-frequency roll motion, but exhibits reduced accuracy at higher-frequency transient events. The Pearson correlation of 0.623 and envelope correlation of 0.606 indicate a moderate correspondence with the reference signal. The NRMSE of 0.782

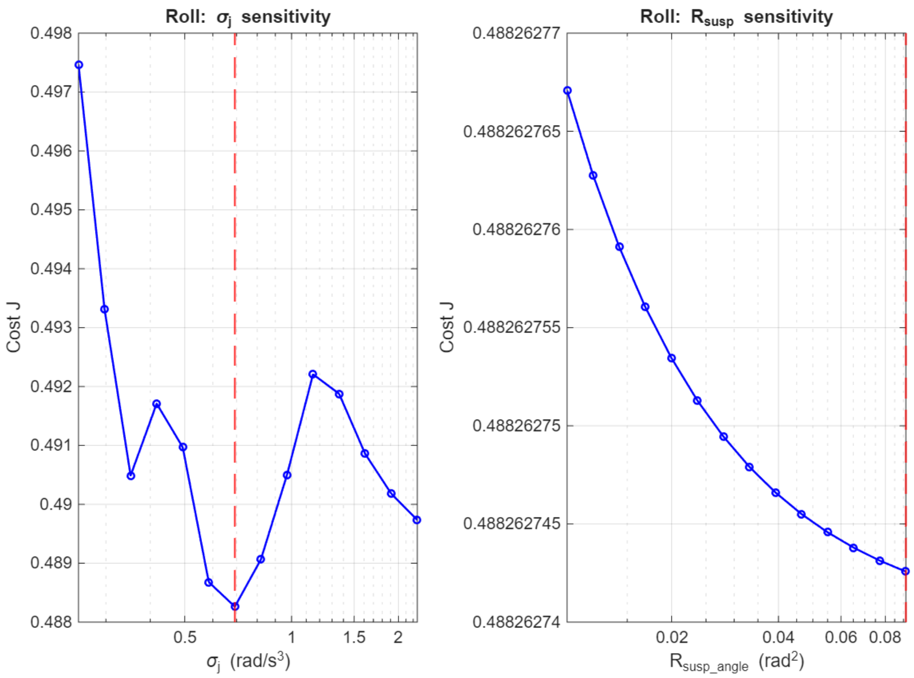

Figure 5.13: One-dimensional cost slices through the optimal roll observer tuning, showing the sensitivity of the cost function to σ_j (left) and R_{susp} (right).

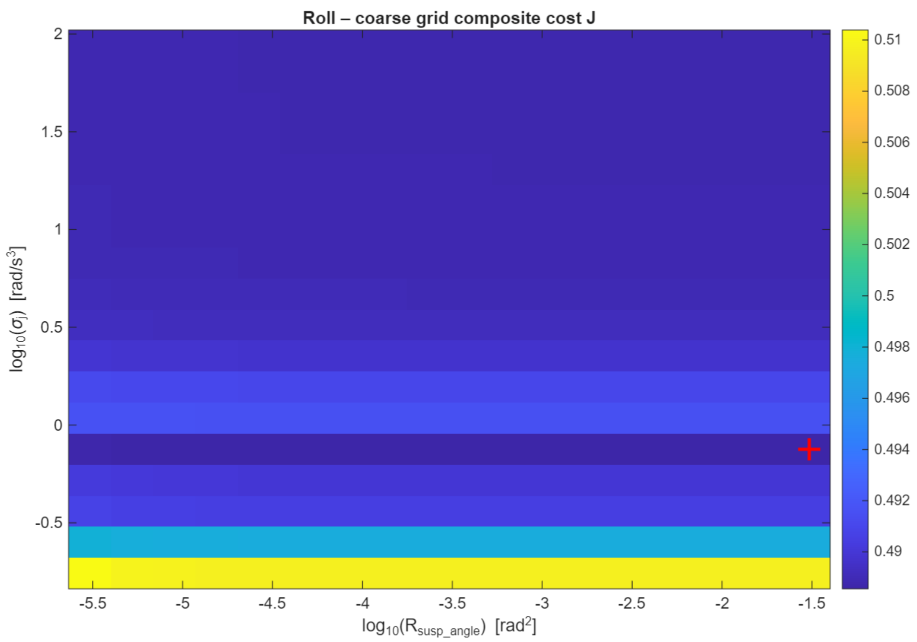

Figure 5.14: Coarse grid-search cost surface for the roll observer. The marker indicates the identified optimal parameter combination.

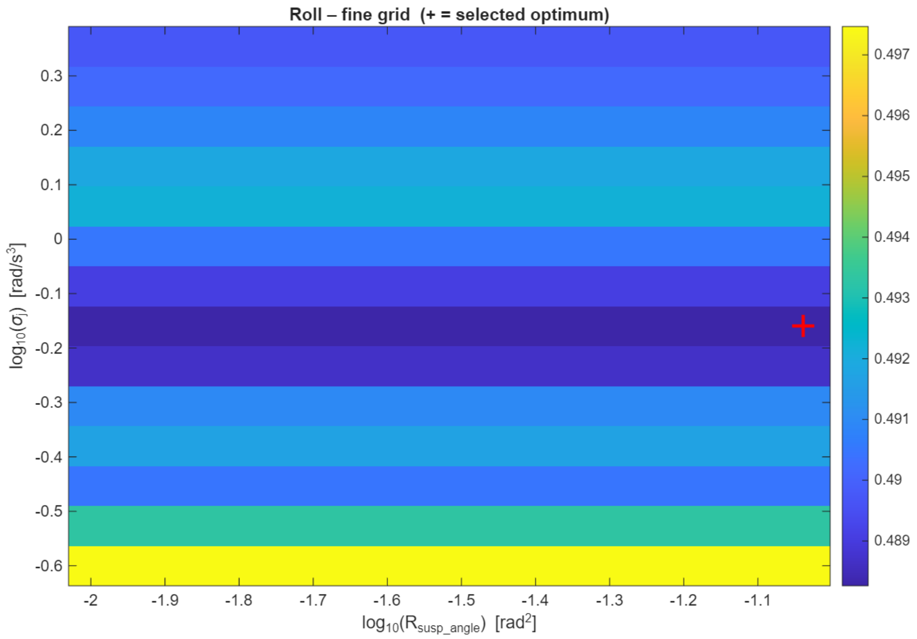

Figure 5.15: Fine grid-search cost surface for the roll observer, zoomed into the neighbourhood of the coarse optimum. The marker indicates the final selected parameter combination.

Table 5.2: Evaluation metrics for the roll and pitch angular acceleration observers. A synchronisation lag of 0.020 s was removed prior to evaluation.

Metric	**Roll**	**Pitch**
RMSE (deg/s^2)	0.1826	0.0469
NRMSE	0.7819	0.3023
Pearson correlation (r)	0.6234	0.9534
Mean phase lag (deg)	19.20	3.48
ISO weighted error (deg/s^2)	0.1506	0.0330
Mean coherence ($\bar{\gamma}^2$)	0.3742	0.8891
Envelope correlation	0.6057	0.9420
Mean NEC (dB)	-1.65	-10.18
Synchronisation lag (s)	0.020	0.020
Tuned σ_j (rad/s^3)	0.6922	0.9977
Tuned R_{susp} (rad^2)	9.14×10^{-2}	1.02×10^{-6}

is notably higher than for heave and pitch, and the mean phase lag of 19° reflects a slower dynamic response.

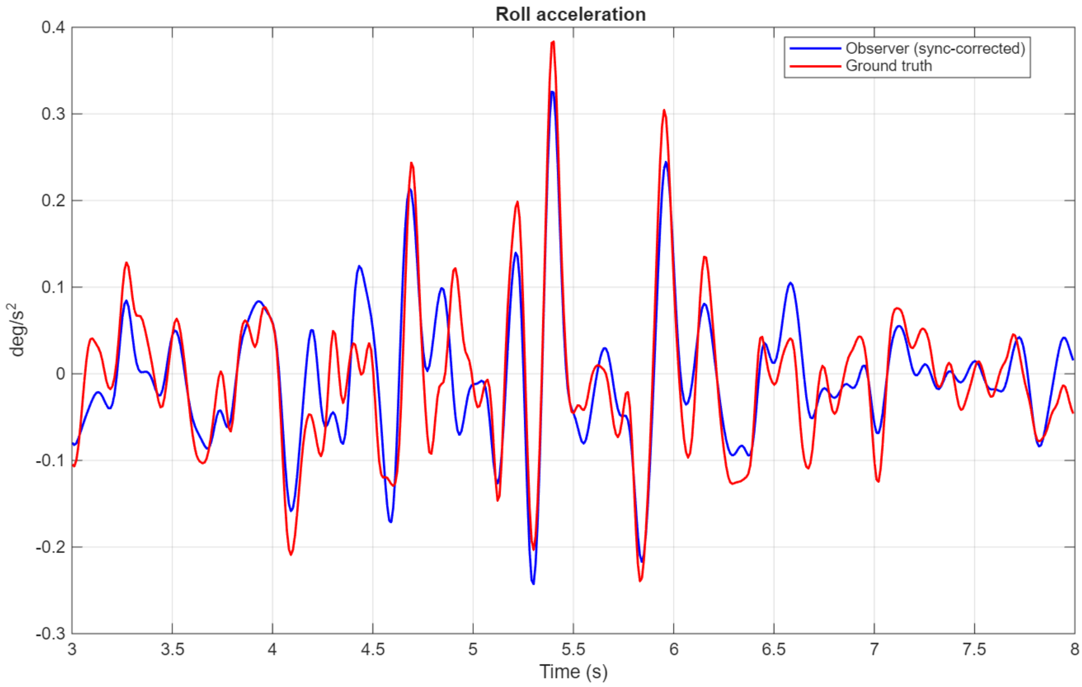

Figure 5.16: Time-domain comparison between the estimated and reference roll angular acceleration signals.

The power spectral density comparison in Figure 5.17 reveals that the estimated roll spectral energy tracks the reference in the low-frequency band but decreases substantially at frequencies above approximately 4–5 Hz. Despite the reduced high-frequency fidelity, the negative NEC value of −1.65 dB confirms that the observer error power remains below the signal power on average. The ISO-weighted roll error of 0.1506 deg/s^2 indicates that the observer continues to capture the most perceptually relevant components of the roll dynamics, even where the broadband metrics suggest moderate agreement.

5.5 Comparative Discussion

Table 5.3 provides a consolidated summary of the key performance metrics across all three observers, enabling a direct comparison of estimation quality for heave, pitch, and roll.

The results reveal a clear performance hierarchy across the three estimation axes. The pitch observer achieves the strongest overall performance, with a Pearson correlation of 0.953 and a mean NEC of −10.18 dB, attributable to the high information content and consistency of the suspension-derived pitch measurement. The heave observer yields intermediate performance, with a correlation of 0.854 and an NEC of −3.37 dB, while the roll observer exhibits the weakest agreement, characterised by a correlation of 0.623 and a shallower NEC of −1.65 dB.

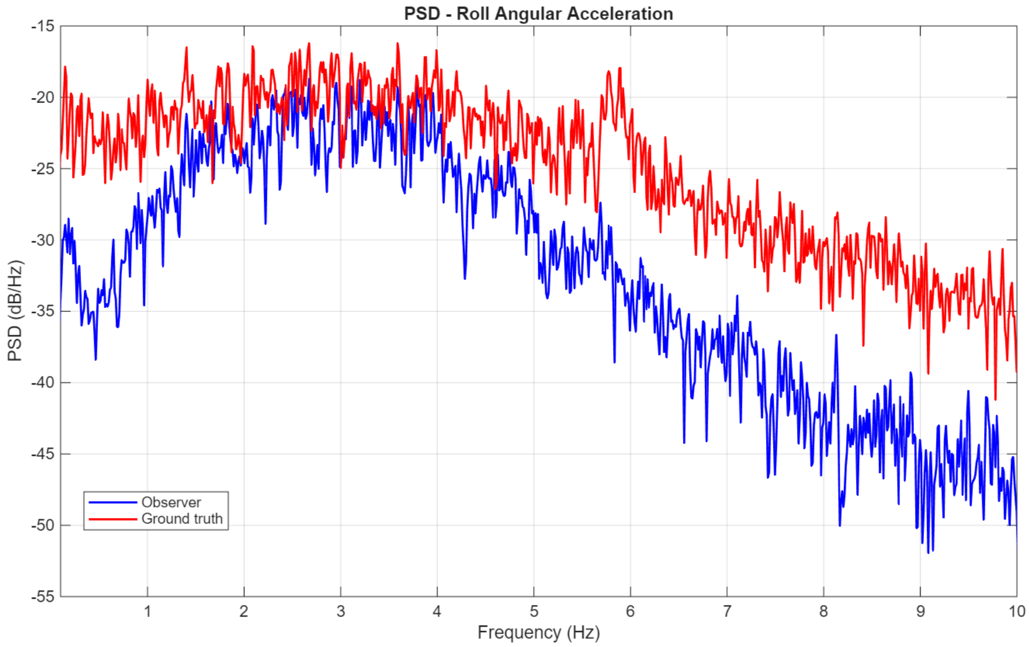

Figure 5.17: Power spectral density comparison between the estimated and ground-truth roll angular acceleration signals.

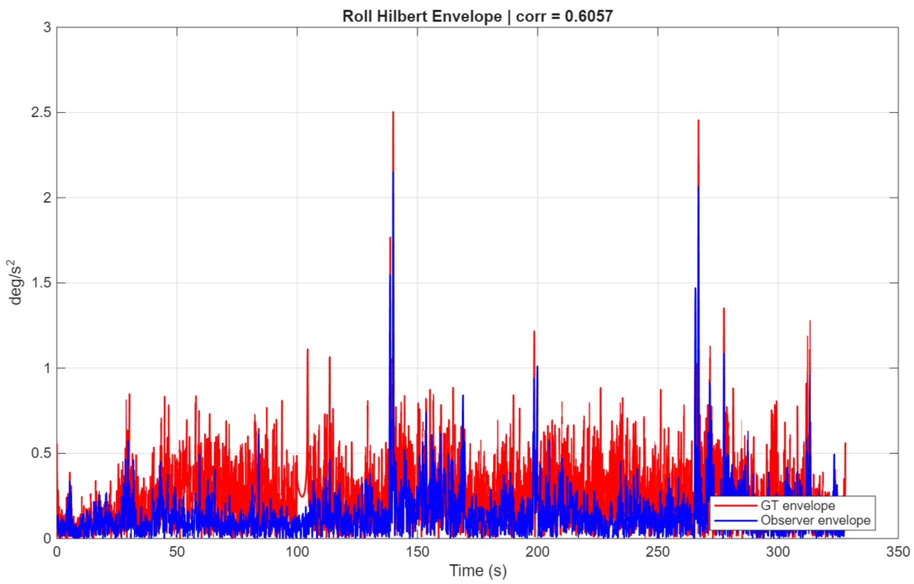

Figure 5.18: Comparison of the Hilbert envelopes of the estimated and reference roll angular acceleration signals.

Table 5.3: Summary of observer performance across all three axes.

Metric	Heave	Pitch	Roll
RMSE	$0.152\,\mathrm{m/s^2}$	$0.047\,\mathrm{deg/s^2}$	$0.183\,\mathrm{deg/s^2}$
NRMSE	0.521	0.302	0.782
Pearson correlation (r)	0.854	0.953	0.623
Mean phase lag (deg)	12.9	3.5	19.2
Mean coherence ($\bar{\gamma}^2$)	0.554	0.889	0.374
Envelope correlation	0.865	0.942	0.606
Mean NEC (dB)	−3.37	−10.18	−1.65
ISO weighted error	$0.090\,\mathrm{m/s^2}$	$0.033\,\mathrm{deg/s^2}$	$0.151\,\mathrm{deg/s^2}$
Optimal cost J	0.321	0.141	0.488

A consistent pattern is observed across all three axes in the frequency domain: the observers reproduce the dominant low-frequency dynamics of the primary ride band with good fidelity, while spectral energy deviates progressively from the reference at higher frequencies. This behaviour can be attributed to two principal factors:

1. **Linear model limitations.** The observer is based on a linearised vehicle model that does not account for suspension nonlinearities, tyre dynamics, load transfer, or higher-order vehicle behaviours. These effects become increasingly significant at higher frequencies, particularly in the secondary ride region (5–25 Hz), where nonlinear phenomena dominate vehicle dynamics. The weaker roll performance is largely a manifestation of this limitation, as roll dynamics are inherently more coupled to nonlinear tyre and suspension interactions than pitch or heave.
2. **Filter frequency attenuation.** The noise-suppression and numerical stability requirements of the Kalman filter introduce effective low-pass behaviour that attenuates rapidly varying dynamics. While this strategy is necessary to prevent noise amplification, it reduces observer sensitivity to high-frequency transient events.

Despite these limitations, the ISO frequency-weighted errors remain substantially lower than the broadband NRMSE values for all three axes, indicating that estimation inaccuracies are concentrated predominantly outside the frequency bands most perceptually significant to vehicle occupants. This characteristic is particularly relevant for suspension control applications, where the ability to accurately reproduce human-sensitive vibration content is of primary practical importance.

Returning to the central research question of this thesis, whether SRS IMU data, combined with existing suspension and speed signals, can replace dedicated body-mounted accelerometers for suspension control, the results support a differentiated answer. For heave and pitch, the proposed framework demonstrates estimation quality that is sufficient for ride-comfort assessment and vehicle dynamics monitoring: the observers reproduce the dominant body motion content with strong waveform fidelity, low phase lag, and ISO-weighted errors that are small relative to the ground-truth signal levels. For roll, the observer captures the dominant low-frequency dynamics but falls short of the accuracy achieved for the other two axes, particularly above 4–5 Hz. This is a consequence of the greater contamination of the suspension-derived roll angle by road inputs and unsprung mass dynamics, combined with the inherently higher nonlinear content of roll motion. Roll estimation therefore remains viable for low-frequency ride monitoring but requires further development, likely through nonlinear modelling or additional sensor inputs, before it can fully replace the dedicated accelerometer for all suspension control functions.

6 Conclusion and Future Work

6.1 Conclusion

This thesis set out to answer a practical question: can the inertial sensors already present in a vehicle's Supplemental Restraint System, combined with existing suspension deflection and speed signals, produce estimates of vehicle body heave, roll, and pitch acceleration that are sufficiently accurate to replace dedicated body-mounted accelerometers in suspension control applications? The results show that the answer is yes for two of the three axes and conditionally promising for the third.

For heave and pitch, the proposed Kalman-filter-based observer framework achieves estimation quality that is directly comparable to the dedicated accelerometer system. The heave observer reproduces the dominant vertical dynamics with a Pearson correlation of 0.854, a mean NEC of $-3.37\,\text{dB}$, and an ISO 2631-1 W_k-weighted error of $0.090\,\text{m/s}^2$ representing less than half the perceptually weighted signal level. The pitch observer performs even more strongly, achieving a correlation of 0.953, a mean NEC of $-10.18\,\text{dB}$, and a phase lag of only $3.5°$, indicating near-exact waveform reproduction with negligible estimation delay. The high confidence that the filter assigns to the suspension-derived pitch angle, reflected in the extremely small optimised variance of $1.02 \times 10^{-6}\,\text{rad}^2$ confirms that the front-to-rear height difference is a reliable and information-rich measurement of body pitching motion that complements the IMU effectively.

The roll observer captures the dominant low-frequency roll dynamics but achieves more moderate overall agreement, with a Pearson correlation of 0.623 and increasing spectral attenuation above approximately 4–5 Hz. The underlying reason is physical rather than algorithmic: the suspension-derived roll angle is strongly contaminated by road cross-slope inputs and unsprung mass dynamics, making it a far noisier measurement than the equivalent pitch signal. The filter responds correctly by assigning low confidence to this measurement, but the consequence is that the observer relies more heavily on the process model and IMU rate signal, limiting its ability to track rapid transient roll events. Roll estimation within the primary low-frequency ride band remains useful, but the axis requires further development before it can fully replace the dedicated accelerometer for all suspension control functions.

Three limitations of the current work should be noted. First, the observer is based on a linearised kinematic model and does not capture suspension nonlinearities, tyre dynamics, or load-transfer effects; these become increasingly important above approximately 5 Hz and are the primary source of high-frequency estimation error. Second, a consistent synchronisation lag of 0.020 s was observed between the estimated and reference signals, which is attributable to inter-ECU communication delays and signal conditioning latency that were outside the scope of this study. Third, the observer parameters were optimised on a single proving-ground dataset, and additional validation across a broader range of vehicles, speeds, and road surfaces is needed before the tuning can be considered robust for production deployment.

Notwithstanding these limitations, the core finding is clear. By repurposing sensors that are already present in the vehicle, the proposed framework can deliver the body motion information that suspension controllers require, without any additional hardware. For two of the three axes this has been demonstrated to a standard that is directly useful for ride-comfort assessment and vehicle dynamics monitoring. This validates the central premise of the thesis: that sensor redundancy and hardware cost reduction in suspension systems are achievable through intelligent fusion of existing onboard measurements.

6.2 Future Work

The findings of this study point toward three directions for future development.

The most immediate opportunity lies in improving the fidelity of the vehicle model underlying the observers. Replacing the current linearised kinematic model with a higher-order representation that captures suspension nonlinearities, tyre dynamics, and load-transfer effects would extend the useful estimation bandwidth into the secondary ride region and is likely to yield the largest improvement in roll performance specifically. Alongside this, nonlinear estimation frameworks such as the Unscented Kalman Filter or Extended Kalman Filter could be evaluated as drop-in replacements for the linear observer structure, provided their additional computational cost remains within the budget of a production ECU.

The second direction concerns the timing and calibration of the sensor signals. A detailed analysis of the inter-ECU communication delays and signal conditioning latency present in the current implementation would allow the observed synchronisation offset of approximately 0.020 s to be characterised, modelled, and compensated explicitly within the filter, rather than removed as a post-processing step. Such an approach could improve the temporal alignment between the estimated and reference signals and reduce phase-related estimation errors. In addition, adaptive or gain-scheduled tuning strategies that automatically adjust filter parameters according to vehicle speed, road surface, and driving manoeuvre would further improve robustness without requiring a separate calibration campaign for each operating condition.

The third direction is validation and integration. The observer has been evaluated on a dataset from a single vehicle under a specific set of proving-ground conditions. Extending the validation to a broader range of vehicles, road types, and manoeuvres is a necessary step toward demonstrating generalisability. The ultimate goal is integration into the production suspension control software, where the observer would operate in real time as a direct replacement for the dedicated accelerometer inputs, and its closed-loop effect on CDC and air spring control quality could be assessed end-to-end.

Bibliography

[1] J. Diebel, “Euler Angles, Unit Quaternions, and Rotation Vectors,” *Technical Report, Stanford University*, 2006.

[2] H. Rehbinder and X. Hu, “Drift-free attitude estimation for accelerated rigid bodies,” *Automatica*, vol. 40, no. 4, pp. 653–659, 2004.

[3] H. Ahmed and M. Tahir, “Accurate Attitude Estimation of a Moving Land Vehicle Using Low-Cost MEMS IMU Sensors,” *IEEE Transactions on Intelligent Transportation Systems*, vol. 18, no. 7, pp. 1723–1739, Jul. 2017.

[4] X. Yun, E. R. Bachmann, and R. B. McGhee, “A simplified quaternion-based algorithm for orientation estimation from earth gravity and magnetic field measurements,” *IEEE Transactions on Instrumentation and Measurement*, vol. 57, no. 3, pp. 638–650, Mar. 2008.

[5] J. Rath and P. Ward, “Attitude estimation using GPS,” *Proc. Nat. Tech. Meeting Inst. Navigat.*, vol. 1, pp. 169–178, 1989.

[6] J. Cho and K. Najafi, “0.00016 deg/$\sqrt{\text{hr}}$ Angle Random Walk (ARW) and 0.0014 deg/hr Bias Instability (BI) from a 5.2M-Q and 1-cm Precision Shell Integrating (PSI) Gyroscope,” in *Proc. 7th IEEE Int. Symp. Inertial Sensors and Systems*, 2020.

[7] Analog Devices, “The Case of the Misguided Gyro,” *Analog Dialogue*, 2017.

[8] M. Shoaib, U. I. Bhatti, A. Bhatti, and S. M. D. Ali, “Improved Attitude Determination by Compensation of Gyroscopic Drift by Use of Accelerometers and Magnetometers,” *Measurement*, 2019.

[9] H. Rahimi, A. A. Nikkhah, and K. Hooshmandi, “A Fast Alignment of Marine Strapdown Inertial Navigation System Based on Adaptive Unscented Kalman Filter,” *International Journal of Control, Automation and Systems*, 2021.

[10] G. Yilmaz, “Design of Attitude Estimation Algorithms for Inertial Sensors Only,” Master’s Thesis, *Middle East Technical University (METU)*, 2022.

[11] G. Chen, J. Yao, Z. Gao, and Z. Gao, “Estimation of Lateral Velocity and Cornering Stiffness in Vehicle Dynamics Based on Multi-Source Information Fusion,” *SAE Int. Journal of Vehicle Dynamics, Stability, and NVH*, 2024.

[12] J. J. Oh and S. B. Choi, “Vehicle velocity observer design using 6-D IMU and multiple-observer approach,” *IEEE Transactions on Intelligent Transportation Systems*, vol. 13, no. 4, pp. 1865–1879, Dec. 2012.

[13] V. R. Marco, J. Kalkkuhl, J. Raisch, and T. Seel, “Multi-modal sensor fusion for highly accurate vehicle motion state estimation,” *Control Engineering Practice*, vol. 99, Art. no. 104409, Jun. 2020, doi: 10.1016/j.conengprac.2020.104409.

[14] Y. Bar-Shalom, X. R. Li, and T. Kirubarajan, *Estimation with Applications to Tracking and Navigation*. New York, NY, USA: John Wiley & Sons, 2001.

[15] D. Dash and J. Valarmathi, “Modeling and Analysis of Velocity, Acceleration and Jerk Models for Tracking Maneuvering Targets,” *International Journal of Pure and Applied Mathematics*, vol. 118, no. 18, pp. 4019–4029, 2018.

[16] J. Ryu, S.-K. Chen, and N. K. Moshchuk, “Estimation of Vehicle Roll Rate and Roll Angle Using Suspension Deflection Sensors,” U.S. Patent Application US 2007/0239320 A1, Oct. 11, 2007.

[17] E. S. Arthur Paul and S. Varadharajan, “Sensor Fusion for Estimating Vehicle Chassis Movement,” Master’s Thesis, *KTH Royal Institute of Technology*, Stockholm, Sweden, 2021.

[18] Y. Luo, Y. Zhu, D. Luo, J. Zhou, E. Song, and D. Wang, “Globally Optimal Multisensor Distributed Random Parameter Matrices Kalman Filtering Fusion with Applications,” *Sensors*, vol. 8, no. 12, pp. 8086–8103, 2008.

[19] A. M. Sabatini, “Quaternion-Based Extended Kalman Filter for Determining Orientation by Inertial and Magnetic Sensing,” *IEEE Transactions on Biomedical Engineering*, vol. 53, no. 7, pp. 1346–1356, Jul. 2006.

[20] J. K. Lee, E. J. Park, and S. N. Robinovitch, “Estimation of Attitude and External Acceleration Using Inertial Sensor Measurement During Various Dynamic Conditions,” *IEEE Transactions on Instrumentation and Measurement*, vol. 61, no. 8, pp. 2262–2273, Aug. 2012.

[21] S. Reymert, Ø. W. Petersen, A. Rönnquist, O. Øiseth, and L. Drugge, “Development and validation of a Kalman filter to identify lateral crosswind loads on road vehicles in real operating environments,” *Mechanical Systems and Signal Processing*, vol. 232, Art. no. 112679, Jun. 2025.

[22] R. E. Kalman, “A New Approach to Linear Filtering and Prediction Problems,” *Transactions of the ASME – Journal of Basic Engineering*, vol. 82, no. D, pp. 35–45, 1960.

[23] International Organization for Standardization, *ISO 8855:2011 Road vehicles — Vehicle dynamics and road-holding ability — Vocabulary*, ISO, Geneva, Switzerland, 2011.

[24] International Organization for Standardization, *ISO 2631-1:1997 Mechanical vibration and shock — Evaluation of human exposure to whole-body vibration — Part 1: General requirements*, ISO, Geneva, Switzerland, 1997.

[25] The author used generative artificial intelligence tools, during the preparation of this thesis to assist with language refinement, proofreading, LaTeX formatting, and code documentation. All technical concepts, methodology development, implementation, analysis, validation, and conclusions were developed, verified, and reviewed by the author. The author takes full responsibility for the content of this thesis.

A

Performance Metric Definitions

This appendix provides the complete mathematical definitions of all performance metrics used in Chapter 5. Let $\hat{s}(n)$ denote the observer output and $s(n)$ the ground-truth reference signal, both evaluated at N discrete time steps $n = 1, \ldots, N$, after synchronisation lag removal.

Time-Domain Metrics

A.0.0.0.1 Root Mean Square Error (RMSE).

$$\mathrm{RMSE} = \sqrt{\frac{1}{N}\sum_{n=1}^{N}\Big(\hat{s}(n) - s(n)\Big)^2}. \tag{A.1}$$

A.0.0.0.2 Normalised RMSE (NRMSE). The RMSE normalised by the RMS of the ground-truth signal:

$$\mathrm{NRMSE} = \frac{\mathrm{RMSE}}{\sqrt{\frac{1}{N}\sum_{n=1}^{N} s(n)^2}}. \tag{A.2}$$

A value of 0 indicates perfect estimation; a value of 1 indicates that the error energy equals the signal energy.

A.0.0.0.3 Pearson Correlation Coefficient (r).

$$r = \frac{\sum_{n=1}^{N}\Big(\hat{s}(n) - \bar{\hat{s}}\Big)\Big(s(n) - \bar{s}\Big)}{\sqrt{\sum_{n=1}^{N}\Big(\hat{s}(n) - \bar{\hat{s}}\Big)^2}\sqrt{\sum_{n=1}^{N}\Big(s(n) - \bar{s}\Big)^2}}, \tag{A.3}$$

where $\bar{\hat{s}}$ and $\bar{s}$ are the respective signal means.

A.0.0.0.4 Envelope Correlation. The Pearson correlation coefficient computed on the Hilbert envelopes $|\mathcal{H}\{\hat{s}\}|$ and $|\mathcal{H}\{s\}|$, where $\mathcal{H}$ denotes the analytic signal obtained via the Hilbert transform. This metric quantifies agreement in instantaneous amplitude modulation independently of waveform phase.

Frequency-Domain Metrics

A.0.0.0.5 Mean Squared Coherence ($\bar{\gamma}^2$). The magnitude-squared coherence at frequency f is

$$\gamma^2(f) = \frac{|P_{\hat{s}s}(f)|^2}{P_{\hat{s}\hat{s}}(f)\, P_{ss}(f)}, \tag{A.4}$$

where $P_{\hat{s}s}(f)$ is the cross-power spectral density and $P_{\hat{s}\hat{s}}(f)$ and $P_{ss}(f)$ are the auto-power spectral densities, estimated using Welch's method. The mean coherence over the evaluation band $[f_{\text{low}}, f_{\text{high}}]$ is reported:

$$\bar{\gamma}^2 = \frac{1}{|F|} \sum_{f \in F} \gamma^2(f). \tag{A.5}$$

A.0.0.0.6 Normalised Phase Lag Ratio (NPLR). The phase angle between $\hat{s}$ and s at frequency f is $\varphi(f) = \angle P_{\hat{s}s}(f)$. The NPLR weights the absolute phase by the ground-truth power and normalises by π:

$$\text{NPLR} = \frac{1}{\pi} \frac{\sum_{f \in F} P_{ss}(f)\, |\varphi(f)|}{\sum_{f \in F} P_{ss}(f)}. \tag{A.6}$$

This metric emphasises phase error at frequencies where the reference signal contains the greatest energy, thereby providing a weighted measure of phase agreement between the estimated and ground-truth signals.

A.0.0.0.7 Normalised Error Power Coefficient (NEC_{lin}).

$$\text{NEC}_{\text{lin}} = \frac{\sum_{f \in F} P_{ee}(f)}{\sum_{f \in F} P_{ss}(f)}, \tag{A.7}$$

where $P_{ee}(f)$ is the PSD of the error signal $e(n) = \hat{s}(n) - s(n)$. The reported value in Chapter 5 is

$$\text{NEC}_{\text{dB}} = 10 \log_{10} \left(\text{NEC}_{\text{lin}}\right). \tag{A.8}$$

Perceptually Weighted Metric

A.0.0.0.8 ISO 2631-1 Frequency-Weighted RMS Error. The ISO 2631-1:1997 [24] W_k weighting filter is applied to the error signal and the RMS of the filtered result is reported. The discrete-time approximation used in this study consists of a cascade of a second-order high-pass filter ($f_1 = 0.4\,\text{Hz}$), a first-order band-pass section ($f_2 = 1\,\text{Hz}$ to $f_3 = 12.5\,\text{Hz}$), and a second-order low-pass filter ($f_4 = 12.5\,\text{Hz}$), with unity gain normalised at $4\,\text{Hz}$. For pitch and roll motions, the same weighting filter is adopted as a practical approximation of the ISO 2631-1 W_e and W_d weightings, owing to their similar pass-band characteristics.

B

Sensor and Hardware Specifications

The specifications presented in Table B.1 correspond to the [redacted] used throughout this study and provide the basis for the sensor noise characterisation adopted in the observer design.

Table B.1: [redacted] key specifications used in the observer design.

Parameter	Value	Notes
Accelerometer axes	[redacted]	
Accelerometer range	[redacted]	Crash-optimised
Accelerometer noise std	[redacted]	Used in $\boldsymbol{\Sigma}_A$
Gyroscope axes	[redacted]	
Gyroscope range	[redacted]	
Gyroscope noise std	[redacted]	[redacted]
CAN output rate	[redacted]	After internal filtering
Signal latency (CAN output)	[redacted]	Source of synchronisation offset

Table B.2: Vehicle geometry parameters used in all three observers.

Parameter	Symbol	Value	Description
CG-to-front-axle	l_f	[redacted]	Longitudinal distance from CG
CG-to-rear-axle	l_r	[redacted]	Longitudinal distance from CG
Front half-track	t_f	[redacted]	Centreline to wheel centre
Rear half-track	t_r	[redacted]	Centreline to wheel centre
Full wheelbase	$l_f + l_r$	[redacted]	Used in pitch-angle geometry
Full track width	$2t_f = 2t_r$	[redacted]	Used in roll-angle geometry

C
Grid Search Parameter Ranges

Tables C.1–C.3 document the parameter ranges used in the two-stage grid-search tuning procedure (Section 5.1). All grids use logarithmically spaced points unless otherwise stated. The cost function J (Equation 5.1) is evaluated at every grid point and the global minimum is selected as the final tuning.

Table C.1: Grid search ranges for the heave observer.

Stage	Parameter	Min	Max	Points	Spacing
Coarse	σ_j (m/s^3)	0.01	10.0	30	Log
Coarse	R_{zb} (m^2)	10^{-7}	10^{-2}	30	Log
Fine	σ_j (m/s^3)	0.3	1.5	25	Log
Fine	R_{zb} (m^2)	10^{-6}	10^{-4}	25	Log

Table C.2: Grid search ranges for the pitch observer.

Stage	Parameter	Min	Max	Points	Spacing
Coarse	σ_j (rad/s^3)	deg2rad(10)	deg2rad(5000)	18	Log
Coarse	R_{susp} (rad^2)	deg2rad(0.1)^2	deg2rad(10)^2	18	Log
Fine	σ_j (rad/s^3)	coarse/3	coarse×3	14	Log
Fine	R_{susp} (rad^2)	coarse/3	coarse×3	14	Log

Table C.3: Grid search ranges for the roll observer (same structure as pitch).

Stage	Parameter	Min	Max	Points	Spacing
Coarse	σ_j (rad/s^3)	deg2rad(10)	deg2rad(5000)	18	Log
Coarse	R_{susp} (rad^2)	deg2rad(0.1)^2	deg2rad(10)^2	18	Log
Fine	σ_j (rad/s^3)	coarse/3	coarse×3	14	Log
Fine	R_{susp} (rad^2)	coarse/3	coarse×3	14	Log

The author used generative artificial intelligence tools to assist with code documentation and language refinement during the preparation of this thesis, as noted in [25]. All methodology development, observer design, implementation, validation, analysis, and interpretation of results were performed by the author.

DEPARTMENT OF SOME SUBJECT OR TECHNOLOGY
CHALMERS UNIVERSITY OF TECHNOLOGY
Gothenburg, Sweden
www.chalmers.se

AVANCEZ
1829

CHALMERS
UNIVERSITY OF TECHNOLOGY